Computation of Protonation Patterns

for Organic Compounds and Transition Metal Complexes

Dissertation zur Erlangung des akademischen Grades des

Doktors der Naturwissenschaften (Dr. rer. nat.)

eingereicht im Fachbereich Biologie, Chemie, Pharmazie

der Freien Universität Berlin

vorgelegt von

Gegham Galstyan

aus Eriwan, Armenien

Berlin, 2014

Die vorliegende Dissertation wurde unter Anleitung von Prof. Dr. E. W. Knapp im Zeitraum 03/2009 – 06/2014 am Institut für Biologie, Chemie und Pharmazie der Freien Universität Berlin durchgeführt.

1. Gutachter: *Prof. Dr. Ernst-Walter Knapp, Freie Universität Berlin*

2. Gutachter: *Prof. Dr. Beate Paulus, Freie Universität Berlin*

Disputation am   *29.10.2014*

P R E A M B L E

This PhD thesis summarizes my research work for the past years related to the computation of protonation patterns in organic compounds and transition metal complexes. The work is written in a partially cumulative fashion, based on the following peer-reviewed journal publication as well as the material not yet published at the time of preparation of this thesis:

1. Galstyan G., Knapp E.W.

   Computations of 36 tautomer/isomer equilibria of different lactams

   Journal of Physical Chemistry A **116**(25): 6885-6893, 2012.

2. Galstyan G., Knapp E.W.

   Computing pK$_A$ values of hexa-aqua transition metal complexes

   Journal of Computational Chemistry, under revision.

   Accepted version: http://dx.doi.org/10.1002/jcc.23764

During my PhD study I also administered our local IT infrastructure at the Macromolecular Modeling Group, involving Linux based computer cluster for grid and GPU computing. Provided technical support & troubleshooting.

During these years I also contributed to the following scientific research, where I performed all quantum chemical computations:

1. Ma L., Galstyan G., Zhang K.K., Kloc C., Sun H.D., Soci C., Michel-Beyerle M.E., Gurzadyan G.G.

   Two-photon-induced singlet fission in rubrene single crystal

   Journal of Chemical Physics **138**(18): 184508/1-184508/6), 2013.

2. Woelke A.L., Galstyan G., Galstyan A., Meyer T., Heberle J., Knapp E.W.

   Exploring the possible role of Glu286 in CcO by electrostatic energy computations combined with molecular dynamics

   Journal of Physical Chemistry B **117**(41): 12432-12441, 2013.

3. Woelke A.L., Kuehne C., Meyer T., Galstyan G., Dernedde J., Knapp E.W.

   Understanding selectin counter-receptor binding from electrostatic energy computations and experimental binding studies

   Journal of Physical Chemistry B **117**(51): 16443-16454, 2013.

4. Woelke A.L., Galstyan G., Knapp E.W.

   Lysine 362 in cytochrome c oxidase regulates opening of the K-channel via changes in pK$_A$ and conformation

   Biochimica et Biophysica Acta – Bioenergetics, 2014, doi: 10.1016/j.bbabio.2014.08.003.

5. Woelke A.L., Wagner A., Galstyan G., Meyer T., Knapp E.W.

   Proton transfer in the K-channel analogue of B-type cytochrome c oxidase from thermus thermophilus

   Biophysical Journal, submitted.

The text of this thesis skips the detailed overview of the formalisms of the quadratic configuration interaction, density functional, and Poisson-Boltzmann continuum electrostatics theories, as well as the numerical techniques for solution of the associated Schrödinger, Kohn-Sham and Poisson-Boltzmann equations extensively used in this work. The detailed description of the least squares procedure for numerical derivation of electrostatic potential charges are also omitted. All these information is very well documented, and an interested reader is recommended to address the comprehensive literature or the manuals of the associated software cited as required in the text of this work.

ACKNOWLEDGEMENTS

I thank all my colleagues and friends for making my stay in Berlin productive and memorable.

C O N T E N T S

ABBREVIATIONS

OEC	oxygen evolving complex
PSII	photosystem II
QCISD(T)	quadratic configuration interaction with single and double excitations and triple excitations added perturbatively
MP2	second-order Møller–Plesset perturbation
RMSD	root-mean-square deviation
DFT	density functional theory
SCF	self-consistent field
CPU	central processing unit
BH&HLYP(G)	modified version of BH&HLYP DFT functional as implemented in Gaussian09
NICS	nucleus-independent chemical shift
QM/MM	quantum mechanics/molecular mechanics
JTE	Jahn-Teller effect
SASA	solvent accessible surface area
RESP	restraint electrostatic potential
EA	electron affinity

1. INTRODUCTION

The combined action of electrons and protons in molecules is an essential component in the lifecycle of biochemical processes found in nature. Therefore, precise knowledge of redox and protonation states of molecules supporting function of biological systems is the key for understanding the basic mechanisms driving life on the earth. In spite of the huge advances in modern experimental technique and equipment, the small size and high mobility of protons and electrons make such observations extremely challenging or even impossible. Hence, the role of scientific theories and hypotheses, based on computational methods for prediction of physicochemical properties of molecules like reduction potential, ionization potential, acid dissociation constant and prototropic tautomerization constant are crucial. Successful application of existing theoretical methods, or the development of new reliable methods for studying complex bio-molecular systems, requires initial proof of their eligibility in reproducing known properties for a set of less complex prototype reference molecules.

Since more than a decade our group is developing *ab initio* approaches for reduction potential and pK_A computations based on a combination of quantum chemical and electrostatic methods that involve computation of gas phase energies and solvation energies of the studied compounds in different protonation states (Schmidt am Busch and Knapp 2004, Schmidt Am Busch and Knapp 2005, Galstyan and Knapp 2009). In such approaches, energies of solvated compounds are computed by summing the energy terms of an appropriate thermodynamic cycle, which connects energy contributions of gaseous and solvated structures. The thermodynamic cycle for a deprotonation process is shown in Scheme 1. Thus, the methods for computation of reduction potential of oxygen-/sulfur-centered organic radicals (Schmidt Am Busch and Knapp 2005) and mononuclear transition metal complexes (Galstyan and Knapp 2009) in protic or aprotic solvents yielded accuracies of 58 mV and 65 mV, respectively. The procedure for pK_A computations (Schmidt am Busch

and Knapp 2004) yielded accuracy of 0.53 pH units for a number of different types of small organic compounds. The aim of this PhD work is to supplement the set of aforementioned methods with appropriate procedures for accurate computation of i) amide-imidic acid and amine-imine tautomerization constants for N-heterocyclic compounds, and ii) acid dissociation constants for hexa-aqua complexes of transition metals. The former may support the understanding of fundamental mechanisms of gene mutations occurring in evolution (Katritzky, Hall et al. 2010), and also be useful for the development of new drugs (Pospisil, Ballmer et al. 2003, Martin 2009, Katritzky, Hall et al. 2010, Milletti and Vulpetti 2010). While the latter will serve as an excellent basis for prediction of protonation states of the oxygen evolving complex (OEC), a Mn_4Ca-cluster center (Robertazzi, Galstyan et al. 2014), which catalyses the process of photosynthetic decomposition of water into electrons, protons and molecular oxygen (Leslie 2009, Cox, Pantazis et al. 2013). This water-plastoquinone oxidoreductase photosystem II (PSII) protein complex (Umena, Kawakami et al. 2011) is used in the thylakoid membrane of plants, algae, and cyanobacteria. Understanding this mechanism of function of the Mn_4Ca-cluster is of technological significance as a source of alternative energy, as well as of fundamental significance for understanding of the detailed mechanism of photosynthesis.

Scheme 1. Thermodynamic cycle for deprotonation process

$$AH_g \xrightarrow{\Delta G_g} A_g^- + H_g^+$$

$$\Delta G_{solv}(AH) \quad \Delta G_{solv}(A^-) \quad \Delta G_{solv}(H^+)$$

$$AH_{aq} \xrightarrow{\Delta G_{aq}} A_{aq}^- + H_{aq}^+$$

$$\Delta G_{aq} = \Delta G_g + \Delta G_{solv}(A^-) + \Delta G_{solv}(H^+) - \Delta G_{solv}(AH)$$
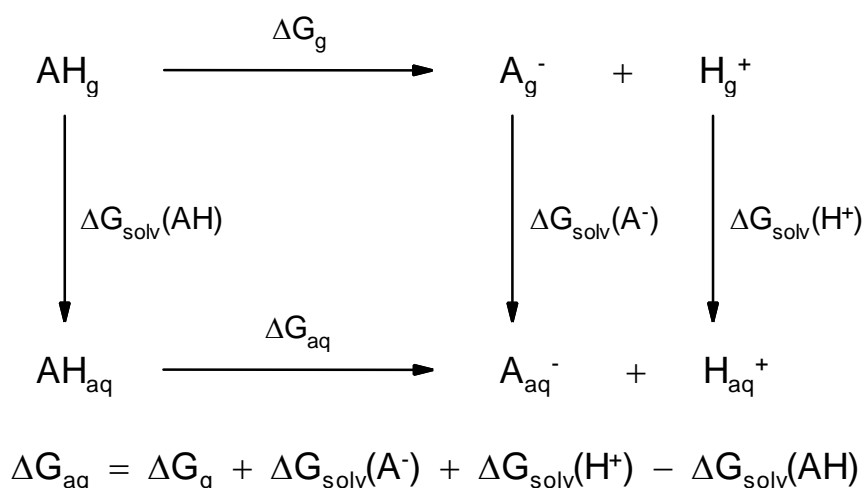
The polarity of the medium surrounding a molecule is one of the main factors influencing tautomer equilibria. Hence, for biological and pharmaceutical applications it is relevant to compute relative energies of tautomers in aqueous (blood or plasma) or non-

protic media (cell membranes or enzymes). Within thermodynamic cycle (Scheme 1) the precision of protonation equilibria will however strongly depend on the quality of tautomer pair energies computed in vacuum. Therefore, finding an appropriate procedure for accurate determination of tautomer equilibria in vacuum is an essential step toward successful computation of tautomer equilibria in different dielectric media.

A recent theoretical work involves a systematic study of the relative energies of tautomer pairs of formamide and six N-heterocyclic compounds (pyridine, four of the primary nucleobases: cytosine, guanine, thymine and uracil; and one non-natural nucleobase: isocytosine) in vacuum (Piacenza and Grimme 2004). Therein the performance of a number of quantum chemical methods was tested in reproducing reference tautomer pair energies computed with the accurate QCISD(T) method [quadratic configuration interaction with single and double excitations and triple excitations added perturbatively] (Pople, Head-Gordon et al. 1987). An improved version of the MP2 method (second-order Møller–Plesset perturbation theory) introduced in (Grimme 2003) yields the smallest root-mean-square deviation (RMSD) of 0.7 kcal/mol. In all computations a basis set of triple-ζ quality was used. For formamide, increasing the quality of the basis set from triple-ζ to pentuple-ζ reduced the discrepancy between the tested and reference methods by 0.3 kcal/mol (Piacenza and Grimme 2004). Interestingly, all considered density functional theory [DFT] (Parr and Yang 1989, Koch and Holthausen 2000) methods underestimated the stability of the lactim relative to lactam tautomer, which the authors assumed to be related to the different aromatic character (aromatic versus non-aromatic) of the two tautomeric forms. They linked this discrepancy to the amount of the exact exchange term in the DFT functional, and suggested that the presence of larger contribution of exchange potential leads to more accurate results. Therefore, it is interesting to study if, there is indeed a correlation between the discrepancy of DFT from QCISD(T) based tautomer pair energies and the difference in aromaticity of two tautomeric states. If such correlation exists, it can be used to build a post-SCF correction scheme, which will provide high quality tautomer pair energies with the less CPU time demanding DFT method. However, to establish such a method accurate reference energies for a larger number of tautomer pairs are required for better statistics. It is also interesting to benchmark the performance in prediction of tautomer pair energies of such promising DFT functionals as recently developed PW6B95

(Zhao and Truhlar 2005); the modified version of the BH&HLYP available in Gaussian09 (Frisch, Trucks et al. 2009), in the following referred to as BH&HLYP(G); and the recently developed empirical post Hartree-Fock localized orbital correction scheme B3LYP-LOC (Friesner, Knoll et al. 2006, Goldfeld, Bochevarov et al. 2008), which is meant to diminish systematic errors made by B3LYP dependent upon the extent of delocalization of the electronic wave function.

Aromaticity of molecules can be characterized quantitatively using the nucleus-independent chemical shift (NICS) tensor (Schleyer, Maerker et al. 1996). The most advanced definition of the scalar value of NICS is the $NICS(0)_{\pi zz}$ index, which is the negative of the magnetic shielding in the center of the ring plane caused by the molecular π-orbitals (Steiner, Fowler et al. 2001, Corminboeuf, Heine et al. 2004). It is derived from the out-of-plane zz-component of the NICS tensor. Much simpler $NICS(1)_{zz}$ aromaticity index is the negative of the magnetic shielding 1 Å above the center of the ring plane, which is derived from the out-of-plane zz-component of the isotropic NICS tensor. The latter serves as a good alternative to the $NICS(0)_{\pi zz}$ index in terms of performance, and it is more readily accessible (Fallah-Bagher-Shaidaei, Wannere et al. 2006).

A set of five measured gas-phase energies of tautomerization, namely for 2-pyridinone, 4-pyrimidinone, 2-pyrazinone and their benzo-fused derivatives is provided by another recent systematic study (Gerega, Lapinski et al. 2007). Availability of accurate measurements is highly important for the estimation of actual capabilities of newly developed computational procedures. A set of accurately measured aqueous pK_A values for hexa-aqua complexes of first and second row transition metals is collected in (Gilson and Durrant 2009).

One precondition for the accurate computation of pK_A values is the accurate computation of gas-phase proton affinities. Like in case with aromatic versus non-aromatic tautomers (Piacenza and Grimme 2004), also when applied to transition metal complexes the DFT is subject to systematic errors depending on the extent of charge delocalization of the electronic wave function (Friesner, Knoll et al. 2006, Knoll and Friesner 2006, Galstyan and Knapp 2009, Jerome, Hughes et al. 2014). This leads to inaccuracies in the estimation of relative energies of compounds with a transition metal in different oxidation states (Galstyan and Knapp 2009, Jerome, Hughes et al. 2014). Appropriate post-SCF correction

schemes are very practical in such cases (Galstyan and Knapp 2009). Similar issues may well be expected when computing relative energies of closed versus open shell systems.

The accuracy of quantum chemical relative energies depends also on the basis set used. It was reported that proton affinities computed with the triple–ζ basis set systematically underestimate measured proton affinities for compounds involving titratable oxygens, while the quadruple–ζ basis set works well (Schmidt am Busch and Knapp 2004).

In two of the most recent studies devoted to the computation of the pK_A values of hexa-aqua transition metal complexes it was reported that the deprotonated species of hexa-aqua complexes with the metal in oxidation state +2 tend to lower the coordination number upon geometry optimization from six to five ligand waters unless explicit solvent water molecules are used (Gilson and Durrant 2009, Jerome, Hughes et al. 2014). The usage of the thermodynamic cycle connecting vacuum and solvation energies (Scheme 1) is based on the assumption that the geometries of molecules in vacuum and in solvent are identical. Therefore, for molecules whose geometries differ considerably in these two phases, a selection of appropriate model geometries may have a strong influence on the accuracy of computed pK_A values. Quantum chemical modeling of solvated geometries by addition of one or only a few explicit waters can be quite arbitrary due to the required decision about initial positions of the solvent molecules. While a sampling over numerous solvent degrees of freedom will dramatically increase the necessary CPU time. In contrast to the latter approach, the combined quantum mechanical – molecular mechanical method [QM/MM] (Warshel and Levitt 1976) can be much more useful to study the influence of explicit solvent on the geometry of a solute molecule since it allows consideration of a large amount of solvent molecules and solvation shells with comparatively low computational cost.

2. P U B L I C A T I O N

Computations of 36 tautomer/isomer equilibria of different lactams

Authors: Galstyan G, Knapp E.W.

Bibliography: Journal of Physical Chemistry A 116, 6885–6893, 2012

Contribution:

- All computations
- Data analysis
- Preparation of the manuscript

In this article the performance of five different DFT (Parr and Yang 1989, Koch and Holthausen 2000) and three QCISD(T) (Pople, Head-Gordon et al. 1987) methods is tested in reproducing measured amide-imidic acid tautomer pair free energies for five 6-membered N-heterocyclic compounds (Fig. 1 of the article) available from (Gerega, Lapinski et al. 2007). Among the DFT methods B3LYP (Vosko, Wilk et al. 1980, Lee, Yang et al. 1988, Becke 1993a, Stephens, Devlin et al. 1994), B3LYP-LOC (Friesner, Knoll et al. 2006, Goldfeld, Bochevarov et al. 2008), BH&HLYP (Lee, Yang et al. 1988, Becke 1993b), PW6B95 (Zhao and Truhlar 2005), and BH&HLYP(G) (Frisch, Trucks et al. 2009) used in conjunction with the cc−pVQZ(-g) basis set (Dunning 1989); and the QCISD(T) method used in conjunction with the cc−pVQZ (Dunning 1989), cc−pVTZ (Dunning 1989, Kendall, Dunning et al. 1992, Woon and Dunning 1993, Woon and Dunning 1994) and 6−31G** (Ditchfie, Hehre et al. 1971, Hehre, Ditchfie et al. 1972, Hehre and Pople 1972, Harihara and Pople 1973, Binkley and Pople 1977, Francl, Pietro et al. 1982) basis sets [denoted as QCISD(T)(q−ζ), QCISD(T)(t−ζ) and QCISD(T)(d−ζ), respectively], the QCISD(T)(q−ζ), BH&HLYP(G) and PW6B95 show excellent agreement with measured values, yielding RMSD of 0.2−0.3 kcal·mol^{-1} (Fig. 2 and Table 1 of the article) Highly accurate but CPU time demanding methods like QCISD(T)(q−ζ) and QCISD(T)(t−ζ) were only used for computation of relatively small molecules involving a single ring. The benchmarking of the considered methods was continued choosing as reference the QCISD(T)(q−ζ) method. Thereby 15 isomer pair energies are computed including 11 amide-imidic acid and 2 amine-imine tautomer pairs, and 2 other isomer pairs, involving one zwitterion. In this comparison the QCISD(T)(t−ζ) method showed overall best accuracy with 0.3 kcal·mol^{-1} RMSD, followed by PW6B59, QCISD(T)(d-ζ), BH&HLYP, B3LYP-LOC methods, each of them with about 0.7 kcal·mol^{-1} RMSD (Fig. 3 and Table 2 of the article). Being superior in reproducing the five mentioned measured pair energies, and well applicable also to zwitterions (in contrast to all other tested DFT methods) the PW6B95 functional was chosen for the further search of correlation between deviation from reference and aromaticity difference for the same 15 isomer pairs used in the benchmarking. Aromaticity of molecules was characterized by the NICS(1)$_{zz}$ value (Schleyer, Maerker et al. 1996) computed by the gauge-independent atomic orbital approach (Wolinski, Hinton et al. 1990) using wave functions computed with the PW91PW91 DFT functional (Perdew, Chevary et al. 1992, Perdew, Chevary et al. 1993) and 6−311G**+ basis set (Krishnan, Binkley et al. 1980,

McLean and Chandler 1980, Clark, Chandrasekhar et al. 1983, Frisch, Pople et al. 1984). An approximately linear correlation between the $NICS(1)_{zz}$ value and the deviation in the tautomer equilibria is obtained (Fig. 4 and eq. 4 of the article), which is used to construct a post Hartree-Fock correction scheme (eq. 5 of the article) for the computation of accurate ground state electronic energies, that allows to reproduce 15 computed reference energies as well as 5 experimental energies, each with an RMSD of 0.5 kcal·mol^{-1}. Corrected relative electronic energies for all 36 tautomer/isomer pairs from Fig. 1 of the article, and corresponding vibrational energies and the $NICS(1)_{zz}$ values are present in the Supporting Information of this article. Gibbs free energies computed for ambient temperature with all considered DFT functionals, as well as B3LYP-LOC correction factors are also given in the Supporting Information of this article.

3. U N P U B L I S H E D   S T U D Y (submitted to the Journal of Computational Chemistry, under revision)

Computing pK$_A$ values of hexa-aqua transition metal complexes

3.1. Studied compounds

The subject of this study are the hexa-aqua transition metal complexes with metals belonging to the first and second transition rows in oxidation states (III) and (II) [Table 1]. Only transition metal complexes, for which reliable measured pK$_A$ values are available [(Gilson and Durrant 2009) and references therein], were considered.

Table 1. Electron configuration and Jahn-Teller distortion (when applicable) for stable spin states of studied complexes.

compound, spin state if ambivalent	electron configuration closed/open [a]	Jahn-Teller distortion [Å] [b]
$[Sc(H_2O)_6]^{3+}$	d^0 (t_{2g}^0 e_g^0) c	
$[Ti(H_2O)_6]^{3+}$	d^1 (t_{2g}^1 e_g^0) o	$-1.4\cdot10^{-3}$
$[V(H_2O)_6]^{3+}$	d^2 (t_{2g}^2 e_g^0) o	$+2.2\cdot10^{-3}$
$[Cr(H_2O)_6]^{3+}$	d^3 (t_{2g}^3 e_g^0) o	
$[Mn(H_2O)_6]^{3+}$ hs	d^4 (t_{2g}^3 e_g^1) o	**+0.212**
$[Fe(H_2O)_6]^{3+}$ hs	d^5 (t_{2g}^3 e_g^2) o	
$[Co(H_2O)_6]^{3+}$ ls	d^6 (t_{2g}^6 e_g^0) c	
$[Co(H_2O)_5OH]^{2+}$ hs	d^6 (t_{2g}^4 e_g^2) o	
$[Ru(H_2O)_6]^{3+}$ ls	d^5 (t_{2g}^5 e_g^0) o	$+1.4\cdot10^{-3}$
$[Rh(H_2O)_6]^{3+}$ ls	d^6 (t_{2g}^6 e_g^0) c	
$[Mn(H_2O)_6]^{2+}$ hs	d^5 (t_{2g}^3 e_g^2) o	
$[Fe(H_2O)_6]^{2+}$ hs	d^6 (t_{2g}^4 e_g^2) o	$+0.04$ [c]
$[Ni(H_2O)_6]^{2+}$	d^8 (t_{2g}^6 e_g^2) o	
$[Zn(H_2O)_6]^{2+}$	d^{10} (t_{2g}^6 e_g^4) c	

[a] **c**: closed shell; **o**: open shell
[b] bond lengths difference between axial and equatorial ligands for vacuum geometries (positive value indicates tetragonal elongation, negative value – compression)
[c] in addition there is 0.01 Å difference in equatorial bond lengths for this complex

Geometries of these metal ions in aqueous solutions have well established six-coordinated octahedral structure, except for Sc(III), which is likely eight-coordinated [(Persson 2010) and references therein]. For the latter complex a six-coordinated geometry is however assumed, which seems to be justified due to the good agreement obtained between computed and measured pK_A values in current work. The energy splitting of the d-orbitals of a central metal ion in an octahedral ligand field is shown in Fig 1. Complexes with an uneven occupation of t_{2g} or e_g orbitals with electrons (see Table 1) are subject to the Jahn-Teller effect [JTE] (Jahn and Teller 1937), which leads to further splitting of t_{2g} and e_g orbitals, giving rise to a distortion of the octahedral symmetry. Four of the 13 considered transition metal complexes possess such uneven occupations of the t_{2g} orbitals, namely $[Ti(H_2O)_6]^{3+}$ $(t_{2g}^{1} e_g^{0})$, $[V(H_2O)_6]^{3+}$ $(t_{2g}^{2} e_g^{0})$, $[Fe(H_2O)_6]^{2+}$ $(t_{2g}^{4} e_g^{2})$ and $[Ru(H_2O)_6]^{3+}$ $(t_{2g}^{5} e_g^{0})$. Here, the JTE leads to only small variations in metal to oxygen distances, since the t_{2g} orbitals are not aligned with the ligands (Table 1). For an uneven occupation of the orbitals e_g, which are directly oriented along the ligand to metal bonds, the JTE is more pronounced. This condition is fulfilled for the complex $[Mn(H_2O)_6]^{3+}$, which possesses a stable high spin $(t_{2g}^{3} e_g^{1})$ electron configuration. Corresponding orbital splitting diagrams for all five configurations are shown in Figs. A1-A5 of the Appendix.
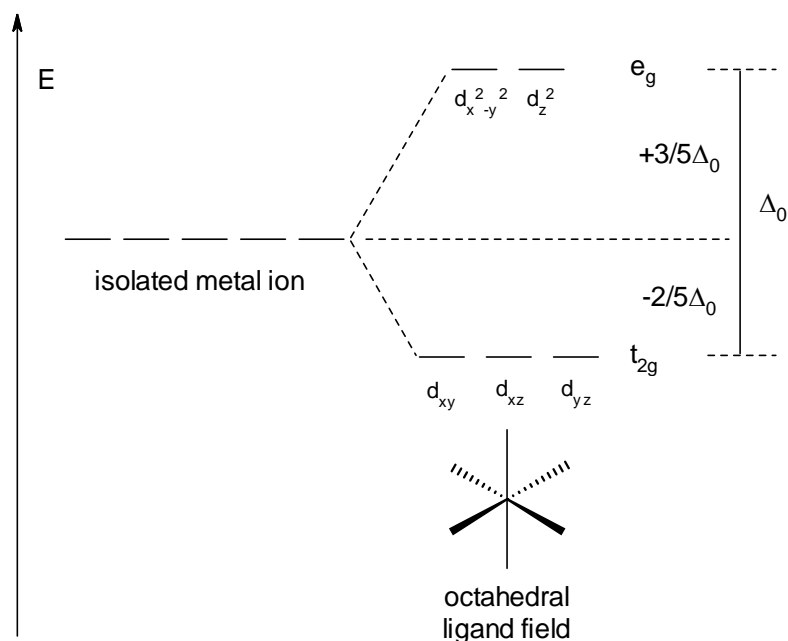
Figure 1. Orbital energy splitting in octahedral ligand field

3.2. Methods

3.2.1. General scheme for computation of pK_A values

The single deprotonation process for hexa-aqua transition metal complexes in water is shown in eq. 1.

$$[M(H_2O)_6]_{aq}^{n+} \longrightarrow [M(H_2O)_5OH]_{aq}^{(n-1)+} + H_{aq}^+ + \Delta G_{aq} \tag{1}$$
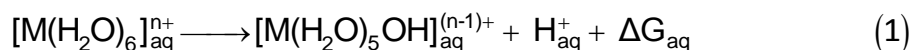
Quantitatively deprotonation is described by the acid dissociation constant K_A, which is related to the free energy change ΔG_{aq} of the process according to eq. 2.

$$pK_A = -lg(K_A) = \frac{\Delta G_{aq}}{2.303 \cdot RT} = \frac{\Delta G_{aq}}{1.364}, \tag{2}$$

where $R = 1.986 \cdot 10^{-3}$ kcal·mol^{-1}·K^{-1} is the molar gas constant (Mohr, Taylor et al. 2012), and $T = 298.15$ K.

The free energy change of deprotonation ΔG_{aq} in aqueous solution is calculated according to the thermodynamic cycle connecting gas and aqueous phase energies (Scheme 2) as shown in eq. 3.

Scheme 2. Thermodynamic cycle for single deprotonation of hexa-aqua transition metal complexes

$$\Delta G_{aq} = \Delta G_g + \Delta\Delta G_{solv}, \tag{3}$$
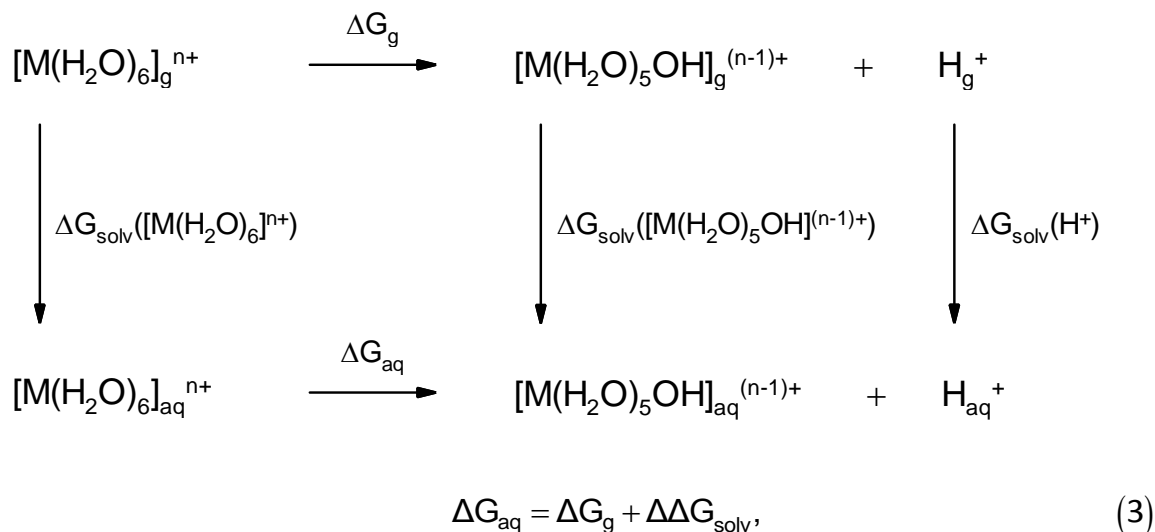
where ΔG_g is the free energy of gas-phase acid dissociation (also referred to as gas phase basicity of the deprotonated species), and $\Delta\Delta G_{solv}$ is the difference in solvation energies of the protonated and deprotonated (including the solvated proton) species.

The gas phase free energy difference is calculated according to eq. 4.

$$\Delta G_g = G_g([M(H_2O)_5OH]^{(n-1)+}) + G_g(H^+) - G_g([M(H_2O)_6]^{n+}), \quad (4)$$

where $G_g(H^+)$ is the free energy of proton in the gas phase, while $G_g([M(H_2O)_5OH]^{(n-1)+})$ and $G_g([M(H_2O)_6]^{n+})$ are the free energies of the related components in vacuum, calculated as the sum of ground state electronic energy $E^0_{electronic}(X)$, zero point vibrational energy $E_{ZPVE}(X)$ and thermal vibrational free energy $G^{298}_{vib}(X)$, as shown in eq. 5.

$$G_g(X) = E^0_{electronic}(X) + E_{ZPVE}(X) + G^{298}_{vib}(X), \quad (5)$$

where X denotes the protonated or deprotonated species of the complex.

The Gibbs free energy of a proton in vacuum is calculated using the convention of statistical thermodynamics, thereby assuming the proton to behave as a mono-atomic ideal gas (McQuarrie 2000), according to eq. 6.

$$G_g(H^+) = H_g(H^+) - TS_g(H^+) = 2.5RT - 0.026012T = 1.48 - 7.76 = -6.28 \text{ kcal} \cdot \text{mol}^{-1}, \quad (6)$$

where $H_g(H^+)$ is enthalpy and $S_g(H^+)$ is entropy [estimated using Sackur–Tetrode equation (McQuarrie 2000)] of proton in gas phase, respectively.

The solvation energy difference in the aqueous phase is calculated according to eq. 7.

$$\Delta\Delta G_{solv} = \Delta G_{solv}([M(H_2O)_5OH]^{(n-1)+}) + \Delta G_{solv}(H^+) - \Delta G_{solv}([M(H_2O)_6]^{n+}), \quad (7)$$

where $\Delta G_{solv}(X)$ are solvation energies of components X in water.

The value for the solvation free energy of proton in water $\Delta G_{solv}(H^+) = -257.98 \text{ kcal} \cdot \text{mol}^{-1}$ is fitted to obtain the best match between computed and measured pK_A values, adopting the procedure used in (Schmidt am Busch and Knapp 2004). It should be noted, that this new value of proton solvation free energy, which works for transition metal complexes, is different from the value $-265.74 \text{ kcal} \cdot \text{mol}^{-1}$ recommended in (Schmidt am Busch and Knapp 2004) for small organic molecules. Both values however stay in the range of measured values varying between -271.7 and -252.6 kcal·mol^{-1} [(Schmidt am Busch and Knapp 2004) and references therein]. The remaining terms in eq. 5 or eq. 7 are computed quantum chemically or by solving the Poisson equation respectively, as described below in the methods part.

Since hexa-aqua complexes possess twelve hydrogen atoms, which are potential candidates for a deprotonation reaction, the measured or macroscopic pK_A will represent the sum of all microscopic $pK_A^{(micro)}$, such that

$$pK_A = -\lg(K_A) = -\lg(12\, K_A^{(micro)}) = pK_A^{(micro)} - 1.1, \tag{8}$$

where $pK_A^{(micro)}$ is computed evaluating eqs. (2) - (7).

3.2.2. Computation of gas-phase basicities

3.2.2.1. Quantum chemical computations

All quantum chemical computations are performed with DFT (Parr and Yang 1989, Koch and Holthausen 2000), using the B3LYP functional (Vosko, Wilk et al. 1980, Lee, Yang et al. 1988, Becke 1993a, Stephens, Devlin et al. 1994). Ground state electronic energies and vibrational frequencies are computed for the isolated transition metal complex geometry optimized either in vacuum or in presence of explicit solvent. The open shell systems were described using the unrestricted, while the closed shell systems using the restricted formalism (see Table 1). The electronic energy of the deprotonated hexa-aqua Co(III) complex was alternatively also computed with the restricted open shell formalism. The inner core orbitals of the transition metals are described using the effective core potential, while the outermost core and the valence orbitals are described by the basis set from the Los Alamos National Laboratory (Hay and Wadt 1985a, Hay and Wadt 1985b). The outermost core and valence orbitals are defined as follows:

Sc – Ni: [core]3s3p3d4s   (Hay and Wadt 1985a)

Zn: [core]3d4s4p   (Hay and Wadt 1985b)

Ru, Rh: [core]4s4p4d5s   (Hay and Wadt 1985a)

Quantum chemical computations in vacuum are performed with Jaguar v7.7 (Bochevarov, Harder et al. 2013, Schrödinger 2010.); QM/MM computations are done using Jaguar v8.3 (Bochevarov, Harder et al. 2013, Schrödinger 2014a) combined with Impact v6.2 (Banks, Beard et al. 2005, Schrödinger 2014b). Geometry optimizations and computation of vibrational frequencies are done using for the atoms H and O the 6−31G**+ basis set (Ditchfie, Hehre et al. 1971, Hehre, Ditchfie et al. 1972, Hehre and Pople 1972, Harihara and Pople 1973, Binkley and Pople 1977, Francl, Pietro et al. 1982). Electronic energy computations are done employing the cc−pVQZ(-g) (Dunning 1989) basis set for H and O atoms and diffuse function for the metal. For comparison purpose the smaller cc−pVTZ (Dunning 1989, Kendall, Dunning et al. 1992, Woon and Dunning 1993, Woon and Dunning

1994) basis set was also used to compute electronic energies, however its accuracy was found to be insufficient. Hence, it was not used in the pK$_A$ computations. The use of symmetry was turned off in all types of computations.

3.2.2.2. Vibrational energies

Vibrational energies are calculated employing the formalism of the statistical thermodynamics, assuming compound X to behave as a poly-atomic ideal gas (McQuarrie 2000). The energies of individual vibrational normal modes, used for these calculations, where computed quantum chemically, as described in the previous section.

The zero-point vibrational energy (in [kcal·mol^{-1}] units) of a poly-atomic ideal gas is calculated as shown in eq. 9.

$$E_{ZPVE}(X) = 0.5 \cdot hc \sum_i \nu_i = 1.429 \cdot 10^{-3} \sum_i \nu_i \; , \tag{9}$$

where h and c denote the Planck constant and speed of light, respectively, and ν_i denotes the energy of i-th normal mode in units of [cm^{-1}].

The thermal vibrational enthalpy in [kcal·mol^{-1}] units (at ambient temperature) is calculated according to eq. 10.

$$H_{vib}^{298}(X) = hc \sum_i \frac{\nu_i}{\exp(\Theta_i/298K) - 1} = 2.857 \cdot 10^{-3} \sum_i \frac{\nu_i}{\exp(4.826 \cdot 10^{-3} \cdot \nu_i) - 1} \; , \tag{10}$$

where $\Theta_i = hc\nu_i / k_\beta = 1.438777 \cdot \nu_i$ is the vibrational temperature of the i-th normal mode in [K] (with ν_i in units of cm^{-1}), and k_β is the Boltzmann constant (Mohr, Taylor et al. 2012).

The thermal vibrational entropy is calculated using eq. 11.

$$S_{vib}^{298}(X) = R \cdot \sum_i \left(\frac{\Theta_i/298K}{\exp(\Theta_i/298K) - 1} - \ln\left(1 - \exp(-\Theta_i/298K)\right) \right) =$$

$$1.986 \cdot 10^{-3} \sum_i \left(\frac{4.826 \cdot 10^{-3} \cdot \nu_i}{\exp(4.826 \cdot 10^{-3} \cdot \nu_i) - 1} - \ln\left(1 - \exp(-4.826 \cdot 10^{-3} \cdot \nu_i)\right) \right), \tag{11}$$

where R = 1.986·10^{-3} kcal·mol^{-1} is the molar gas constant (Mohr, Taylor et al. 2012).

Resulting thermal vibrational free energy at ambient temperature is calculated as follows

$$G_{vib}^{298}(X) = H_{vib}^{298}(X) - 298K \cdot S_{vib}^{298}(X) \tag{12}$$

The total vibrational energy is then obtained by summing up eqs. (9) and (12). The values of fundamental physical constants and unit conversion factors used in eqs. (9) - (12) are adopted from (Mohr, Taylor et al. 2012).

3.2.3. Geometries of transition metal complexes

Three different types of geometry models for the transition metal complexes are considered (Table 2), namely optimized quantum chemically: (i) in vacuum with no constraints, (ii) in vacuum constraining the (O-metal-O) bond angles of nearest neighbor ligands to 90°, and (iii) in presence of explicit water using QM/MM approach (Warshel and Levitt 1976).

Table 2. Different approaches to compute geometries and partial charges of studied compounds.

oxidation state of metal	optimized geometries in	environment for charges
(III)	vacuum	vacuum
	vacuum	implicit water [a]
	explicit water [b]	vacuum
(II)	vacuum [c]	not considered [c]
	vacuum&constr [d]	implicit water [a]
	explicit water [b]	vacuum
	explicit water [b]	implicit water [a]

[a] charges are computed in presence of dielectric continuum with $\varepsilon = 80$
[b] geometries are optimized in explicit water using the QM/MM approach
[c] charges are not considered due to inappropriate geometries for description of deprotonated complexes
[d] geometries are optimized in vacuum constraining (O−metal−O) bond angles between neighbor ligands to 90°

3.2.3.1. Vacuum geometries without constraints

The deprotonated transition metal (II) complexes geometry optimized in vacuum without constraints show formation of strong intramolecular H-bonds between the oxygen of the deprotonated water ligand and the hydrogens of two neighbor water ligands (Fig. 2a). This is due to notable deviation of nearest neighbor (O-metal-O) bond angles from 90°. Such geometries are likely valid in vacuum, but do not apply to aqueous environment, where the formation of intramolecular H−bonds is prevented by the more favorable intermolecular H−bonds between the waters of the coordination shell and first solvation shell. These geometries are not considered in the following. Instead, special constraints are applied to obtain proper geometries for the transition metal (II) complexes as described in the next section.

26
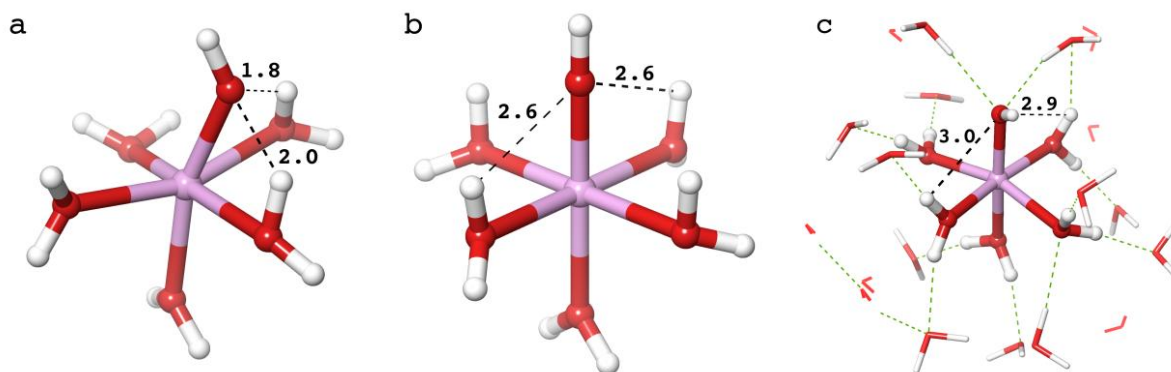
Figure 2. Geometries of deprotonated hexa-aqua Mn(II) complex, optimized in vacuum **a:** without constraints, **b:** constraining the (O-Mn-O) bond angles between nearest neighbor ligands to 90°, and **c:** in presence of explicit solvent using the QM/MM approach. Lengths of the two shortest intramolecular hydrogen bonds are shown in [Å]. For the QM/MM model solvent waters within 3 Å distances of ligand atoms are shown.

In contrast to the transition metal (II) complexes, the transition metal (III) complexes do not exhibit formation of strong intramolecular H-bonds, since the d-orbitals in the latter case impose stronger directionality on the relative positions of the ligands. The nearest neighbor (O-metal-O) bond angles in deprotonated transition metal (III) complexes stay very close to 90°, similar to protonated species. Such geometries serve as good models for the solvated structures of the transition metal (III) complexes, and will be used in the following.

3.2.3.2. Vacuum geometries with constraints

To obtain appropriate geometries for the deprotonated transition metal (II) complexes in vacuum, that are free of strong intramolecular H-bonds, the (O-metal-O) bond angles between nearest neighbor ligand pairs were constrained to 90° during geometry optimization (Fig. 2b). As a result 2 to 3 of the lowest frequency modes from the $3N_{atom} - 6$ vibrational modes ($N_{atom} = 18$ atoms in a deprotonated complex) have imaginary frequency values. Note that the contribution of the lowest frequency vibrational modes to the zero point vibrational energy is negligible. The contribution to thermal vibrational energies from these low frequency modes virtually does not depend on the frequency, since the energy spacing is small such that at room temperature many vibrational states of such modes are occupied. Hence, the contributions of these vibrational modes to the total energy of the

complex can be safely approximated using for each of these modes the energy of the vibrational mode with the lowest real numbered frequency (Table A1 in the Appendix).

3.2.3.3. Geometries with explicit solvent

To consider the influence of the solvent environment on the structure of the transition metal complexes, geometry optimization was also performed in presence of explicit solvent employing the QM/MM approach (Warshel and Levitt 1976). The solvent was represented as a box with TIP3P type water molecules (Jorgensen, Chandrasekhar et al. 1983, Jorgensen, Maxwell et al. 1996, Kaminski, Friesner et al. 2001) with an edge length of 28 Å. The metal ion and the six waters of coordination sphere were described quantum chemically, while all other water molecules were described classically. The structures obtained in vacuum were used as starting geometries (thereby for deprotonated transition metal (II) complexes vacuum geometries with bond angle constraints are used). The water box was generated in presence of the complex, utilizing the module Soak of the program Impact (Banks, Beard et al. 2005, Schrödinger 2014b). Subsequently, the solvent waters were energy minimized with Impact using periodic boundary conditions and fixing the atomic coordinates of the complex. The resulting geometry was used as starting point for the QM/MM computations, where the position of the metal ion was fixed at the center of the water box. For the QM/MM computations periodic boundary conditions were not available in the software. Therefore, normal solvent pressure during QM/MM geometry optimization was ensured by fixing the atomic coordinates of the oxygens belonging to the water molecules of the MM part, whose distance to the nearest atom of the complex is larger than 6 Å. Thereby, only the waters belonging to the first three solvation shells were fully relaxed. The isolated transition metal complexes taken from the QM/MM approach (Fig. 2c) possess no imaginary frequencies.

For the deprotonated Mn(II) and Ni(II) complexes, the water molecules in the first solvation shell had a tendency to be unevenly distributed, which is likely an artifact. To avoid this I started for these two complexes with the geometry of the water box containing Zn(II), which has metal to oxygen bond length intermediate between Mn(II) and Ni(II) (see Tables A2 and A3 in the Appendix).

3.2.4. Computation of solvation energies

3.2.4.1. Poisson equation and electrostatic energy

The solvation of hexa-aqua complexes was described using an implicit solvent model. A schematic view of such a system is shown in Fig. 3. This is an extension of the Debye-Hückel model (Debye and Hückel 1923), where the central region is a single ion. The electrostatic potential $\phi(\mathbf{r})$ in this inhomogeneous dielectric medium is defined by the charge density $\rho(\mathbf{r})$ according to the Poisson equation, which is shown in eq. 13 in atomic units:

$$\nabla \cdot [\varepsilon(\mathbf{r})\nabla\phi(\mathbf{r})] = -4\pi[\rho_A(\mathbf{r}) + \rho_B(\mathbf{r}) + \rho_C(\mathbf{r})], \qquad (13)$$

where dielectric constant ε depends on the region, such that in the volume of the solute (denoted with A) $\varepsilon = 1$, while in the bulk water including also the ion exclusion layer (regions B and C) $\varepsilon = 80$. Thereby vector $\mathbf{r}$ denotes a spatial coordinate of interest.
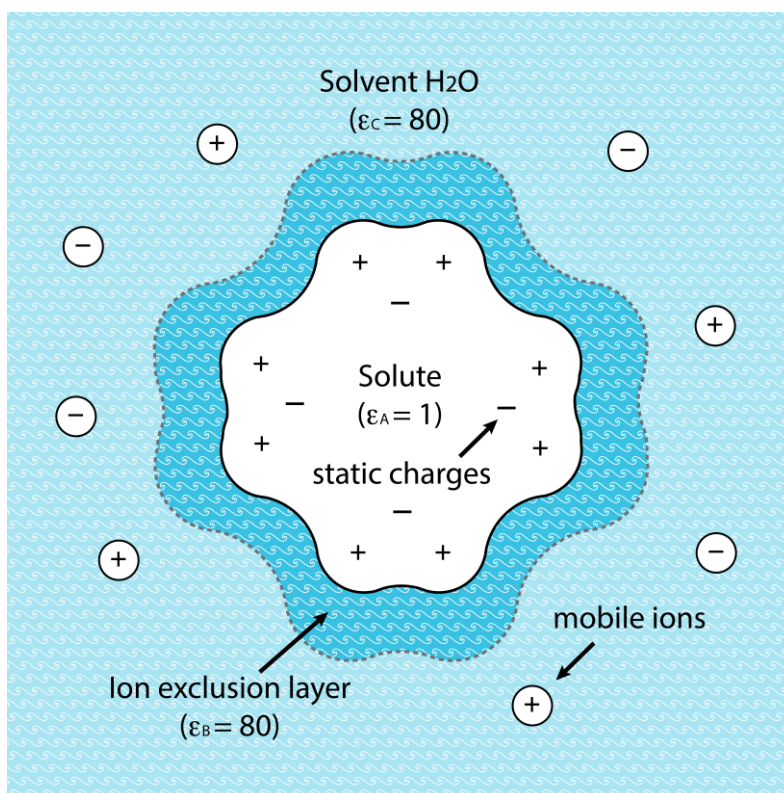
Figure 3. Two-dimensional schematic representation of the implicit solvent model

The charge density in the interior of a solute molecule is defined as the sum over all atomic point charges q_N

$$\rho_A(\mathbf{r}) = \sum_N q_N \delta(\mathbf{r} - \mathbf{r}_N), \tag{14}$$

where δ is the Dirac delta function, and $\mathbf{r_N}$ is the spatial coordinate of the point charge q_N.

The charge density in the ion exclusion layer is $\rho_B(\mathbf{r}) = 0$, due to absence of charges in that volume. The charge density in the bulk solvent is conditioned by the presence of the solvated mobile counter ions, which are subject to the Boltzmann distribution law as assumed in the Debye-Hückel theory. Hence

$$\rho_C(\mathbf{r}) = \sum_J c_J q_J \exp[-q_J \phi(\mathbf{r})/k_\beta T], \tag{15}$$

where c_J and q_J are the concentration and the charge for a given ion J, respectively; k_β is the Boltzmann constant and T is the absolute temperature.

Eq. 15 can be linearized following the approach of Debye and Hückel. In case the electrostatic energy of a given ion J is considerably smaller than its kinetic energy (i.e. $q_J \phi(\mathbf{r})/k_\beta T \ll 1$), eq 15 can be safely approximated by expanding the exponential function in a Taylor series and restricting it to the first two terms

$$\rho_C(\mathbf{r}) \approx \sum_J c_J q_J - \left(1/k_\beta T\right) \sum_J c_J q_J^2 \phi(\mathbf{r}). \tag{16}$$

The condition $q_J \phi(\mathbf{r})/k_\beta T \ll 1$ applies well to mobile ions J located far enough from the solute, such that the eq. 16 describes diluted ionic solutions sufficiently well. Assuming the source of mobile ions J in solution is a 1:1 type electrolyte, the first term of eq. 16 vanishes ($\sum_J c_J q_J = 0$), and the eq. 13 adopts a simpler linear form of the Poisson-Boltzmann equation

$$\nabla \cdot [\varepsilon(\mathbf{r}) \nabla \phi(\mathbf{r})] - (8\pi/k_\beta T) I(\mathbf{r}) \phi(\mathbf{r}) = -4\pi \rho(\mathbf{r}), \tag{17}$$

where

$$I(\mathbf{r}) = 0.5 \sum_J c_J q_J^2 \tag{18}$$

is the ionic strength of the solution.

   The boundary between the solute molecule and the bulk solvent (Fig. 3) is defined by the molecular surface, which is constructed following an original idea of Lee and Richards (Lee and Richards 1971) by rolling a probe sphere of solvent-size (1.4 Å radius for water) over the solute molecule whose shape is represented by the united volume of all atomic van

der Waals (vdW) spheres (Fig. 4). Corresponding vdW radii for ligand water are 1.4 Å for oxygen and 1.0 Å for hydrogen taken from (Schmidt am Busch and Knapp 2004) and (Galstyan and Knapp 2009), respectively. The vdW radii for the metal ions Sc, Ti, V, Cr, Mn, Fe, Co, Ni, Zn, Ru and Rh equal to 1.647, 1.587, 1.572, 1.511, 1.480, 1.456, 1.436, 1.417, 1.381, 1.481 and 1.464 Å, respectively, are adopted from the dataset of the program Jaguar (Bochevarov, Harder et al. 2013, Schrödinger 2010., Schrödinger 2014a).

The solution of the Poisson-Boltzmann equation (eq. 17) yields the electrostatic potential for a given charge distribution of a solute in a given dielectric medium. The resulting electrostatic potential can then be used to calculate the electrostatic energy G_{elstat}, which is defined as the energy required for charging of the atomic point charges of the molecular system from 0 to their full values.

$$G_{elstat} = 0.5 \int_V \rho(\mathbf{r})\phi(\mathbf{r})\,d\mathbf{r}, \tag{19}$$
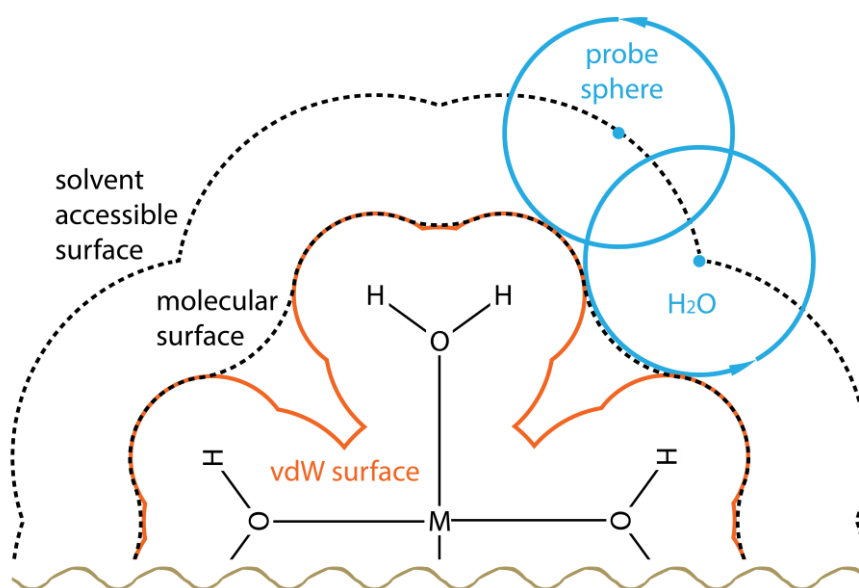
Figure 4. Two-dimensional fragment showing the construction of molecular and solvent accessible surfaces by rolling a probe sphere over the vdW surface of a hexa-aqua complex

3.2.4.2. Solvation energies

The free energy of solvation ΔG_{solv} consists of three major components: electrostatic energy (ΔG_{elstat}) and van der Waals energy (ΔG_{vdW}) of interactions between the solute and

the solvent, as well as cavitation energy (ΔG_{cav}), which is the entropic penalty for reorganization of the solvent molecules around the solute.

$$\Delta G_{solv} = \Delta G_{elstat} + \Delta G_{vdW} + \Delta G_{cav}, \tag{20}$$

The latter two terms are proportional to the solvent accessible surface area [SASA] (Fig. 4), such that

$$\Delta G_{vdW} + \Delta G_{cav} = \beta SASA, \tag{21}$$

where β is an empirical constant.

The electrostatic energy contribution is normally the largest in magnitude among all terms in eq. 20. Having different signs, in the sum (eq. 21) the two energy terms ΔG_{cav} and ΔG_{vdW} partially compensate. Nevertheless, in certain systems, especially those with uncharged and non-polar molecules, the contribution from eq. 21 may become significant, and has to be accounted, if the goal is to compute absolute solvation energies. For the computation of pK_A values, however, one is rather interested in the difference in solvation energies of protonated and deprotonated species, whose SASA values are practically equal, since they differ only with respect to one proton. Therefore, in the energy difference the contributions of vdW and cavitation energies vanish and won't be considered in the following, assuming eq. 22.
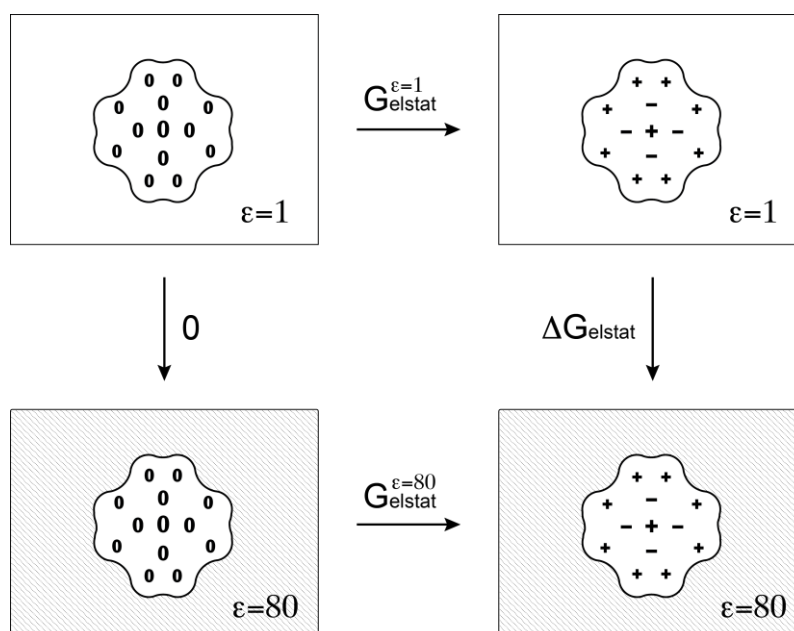
Figure 5. Thermodynamic cycle used in electrostatic energy computations for solvation

32

$$\Delta\Delta G_{solv} = \Delta\Delta G_{elstat} \tag{22}$$

The remaining electrostatic term ΔG_{elstat} is calculated for individual molecules as the difference in energies of the charging process (eq. 19) computed in solvent ($\varepsilon = 80$) versus vacuum ($\varepsilon = 1$). Thereby the thermodynamic cycle shown in Fig. 5 is used.

$$\Delta G_{elstat} = G_{elstat}^{\varepsilon=80} - G_{elstat}^{\varepsilon=1} \tag{23}$$

The Poisson equation (eq. 17 with $I(\mathbf{r})=0$) was solved numerically by finite-difference method using the program Solvate from the program suit MEAD (Bashford and Gerwert 1992, Bashford, Case et al. 1993). Atomic partial charges used for these computations are derived from the quantum chemical wave functions, as described in the next section.

3.2.4.3. Atomic partial charges

Partial charges q_N (eq. 14) at the atomic centers used for electrostatic energy computations were generated using the restraint electrostatic potential (RESP) fitting procedure (Bayly, Cieplak et al. 1993, Cornell, Cieplak et al. 1993). This procedure begins with a quantum chemical evaluation of the molecular electrostatic potential $\phi(\mathbf{r})$ at a large number of grid points located in the neighborhood of the solute, employing eq. 24.

$$\phi(\mathbf{r}) = \phi_{nuc}(\mathbf{r}) + \phi_{el}(\mathbf{r}) = \sum_N Z_N / |\mathbf{R_N} - \mathbf{r}| - \int_V \rho_{el}(\mathbf{r'}) / |\mathbf{r'} - \mathbf{r}| d\mathbf{r'}, \tag{24}$$

where $\phi_{nuc}(\mathbf{r})$ and $\phi_{el}(\mathbf{r})$ are the contributions to the electrostatic potential due to the nuclei and the electrons, respectively. Z_N is the charge of the nucleus N located at the position $\mathbf{R_N}$, while $\rho_{el}(\mathbf{r'})$ is the electron density at position $\mathbf{r'}$.

These points are selected outside the vdW surface of the molecule, which are relevant for the interaction between solute and solvent (Singh and Kollman 1984). For this reason the atomic partial charges for the buried atoms in molecules are often poorly determined, in contrast to the charges of the solvent exposed atoms. As a result a set of reference electrostatic potential values ϕ_i^{ref} is obtained at spatial points i.

In the next step a least square problem is solved to obtain a set of point charges q_N at the atom centers $\mathbf{r_N}$ of the molecule, where the sum of all q_N is constraint to the total molecular charge. The fitting error function χ^2 defined by

$$\chi^2 = \chi^2_{esp} + \chi^2_{rstr}, \tag{25}$$

is minimized.

χ^2_{esp} is the variance between electrostatic potentials computed at spatial points $\mathbf{r}_i$ quantum chemically ϕ_i^{ref} or based on the modeled point charges ϕ_i^{calc} (eq. 26), as shown in eq. 27.

$$\phi_i^{calc} = \sum_N q_N / |\mathbf{r_i} - \mathbf{r_N}|, \tag{26}$$

$$\chi^2_{esp} = \sum_i (\phi_i^{ref} - \phi_i^{calc})^2, \tag{27}$$

χ^2_{rstr} is the penalty function of a hyperbolic form, which is meant to moderate the magnitude of numerically poorly defined fitted charges due to near linear dependencies.

$$\chi^2_{rstr} = a \sum_N (\sqrt{q_N^2 + b^2} - b), \tag{28}$$

where parameter b defines the shape of the hyperbola, and a is the relative weight with respect to the error term χ^2_{esp}.

The criterion for the minimum of χ^2 is

$$\frac{\partial(\chi^2)}{\partial q_N} = \frac{\partial(\chi^2_{esp})}{\partial q_N} + \frac{\partial(\chi^2_{rstr})}{\partial q_N} = 0, \quad \text{for all atomic centers N} \tag{29}$$

The problem is solved iteratively until self-consistency is reached (Bayly, Cieplak et al. 1993).

3.2.4.4. Quantum chemical electrostatic potentials

The electrostatic potentials used for charge fitting, described in the previous section, were derived from the wave functions computed in vacuum ($\varepsilon = 1$) using the B3LYP DFT functional (Vosko, Wilk et al. 1980, Lee, Yang et al. 1988, Becke 1993a, Stephens, Devlin et al. 1994). Atoms of ligands were described by the 6−31G* basis set (Ditchfie, Hehre et al. 1971, Hehre, Ditchfie et al. 1972, Hehre and Pople 1972, Harihara and Pople 1973, Binkley and Pople 1977, Francl, Pietro et al. 1982). The inner core electrons of the transition metals were described by the Los Alamos ECP, while the remaining electrons are described by the basis set available from the same lab (Hay and Wadt 1985a, Hay and Wadt 1985b). To describe the influence of the implicit water, electrostatic potentials were alternatively also evaluated using the wave functions computed in presence of dielectric continuum with $\varepsilon = 80$. To moderate the polarization of water ligands in presence of the dielectric medium the reduced basis set 6−31G was used to describe the oxygen atoms. These two types of quantum chemical electrostatic potentials in line with the three different geometry models of the complexes (described before) lead to the variety of different approaches, used for

computation of the atomic partial charges, summarized in Table 2. Symmetry was not imposed in all these computations.

A note has to made here regarding the smaller basis set (6-31G*) used for vacuum conditions in this work as compared to the 6−31G** basis set used in the earlier works from our lab (Schmidt am Busch and Knapp 2004, Schmidt Am Busch and Knapp 2005, Galstyan and Knapp 2009). Charges derived with the latter basis set yielded accurate pK_A values for a number of small organic molecules (Schmidt am Busch and Knapp 2004). There it was also discussed that the usage of dielectric continuum to evaluate the wave function would lead to electron leakage. I.e. electron density moves into the dielectric medium, thus leading to molecular species which are too polar. Seemingly, even under vacuum conditions, for transition metal complexes the usage of large basis sets can lead to such artifacts. In the present application the charges were evaluated using the smaller basis set to obtain good agreement with the measured pK_A values. Successful application of the charges derived using the 6−31G** basis set in (Galstyan and Knapp 2009), for computation of the reduction potentials of transition metal complexes may well be conditioned by the post Hartree-Fock correction scheme, which might have compensated for the probable artifact of the electron leakage.

3.3. Results and Discussion

3.3.1. Atomic partial charges

Atomic partial charges have been computed for the three different geometry models of the complexes using wave functions generated under vacuum conditions ($\varepsilon = 1$) or in presence of implicit solvent ($\varepsilon = 80$), leading to combinations shown in Table 2. The simplest structure model is obtained by optimizing the complex geometry in vacuum. This model is used for the transition metal (III) complexes and for the protonated form of the transition metal (II) complexes. For the deprotonated form of the transition metal (II) complexes this model is inappropriate due to the formation of strong intra-molecular H-bonds, as has been explained before. For the deprotonated transition metal (II) complexes the structures are

modeled constraining the (O-metal-O) bond angles between nearest neighbor ligands to 90° during geometry optimization in vacuum. Alternatively structures of the transition metal (III) and (II) complexes were also modeled in presence of explicit solvent using the QM/MM approach (Warshel and Levitt 1976).

3.3.1.1. Transition metal (III) complexes

The atomic partial charges for vacuum geometries of the transition metal (III) complexes computed for vacuum ($\varepsilon = 1$) and implicit water (dielectric continuum with $\varepsilon = 80$) environment are listed in the top and bottom parts of Table A4 of the Appendix, respectively. For the protonated complexes the charges of water ligands systematically overestimate the charge polarity of TIP3P bulk water (Jorgensen, Chandrasekhar et al. 1983, Jorgensen, Maxwell et al. 1996, Kaminski, Friesner et al. 2001), i.e. the charges obtained for the oxygen and hydrogen atoms are larger in magnitude than -0.8 and 0.4, respectively. This behavior is less pronounced, if the charges are computed in presence of implicit water than in vacuum conditions, since in the former case a smaller basis set was used that diminished polarization effects. Due to the same reason no clear trend can be observed for the deprotonated complexes (Table A4).

The atomic partial charges for QM/MM geometries of the transition metal (III) complexes computed under vacuum condition ($\varepsilon = 1$) and in presence of implicit water ($\varepsilon = 80$) are listed in Table A5 of the Appendix. Here too, water ligands of the protonated species are more polar compared to bulk water. The differences in the charges of water ligands of the protonated complexes, generated in vacuum versus in presence of implicit solvent, are less pronounced for the QM/MM geometries than for the vacuum geometries (Table A5). In contrast to the vacuum geometries, the charges of the hydrogen atoms in QM/MM geometry model are slightly more polar for the implicit water charge model than for the vacuum charge model. As for the vacuum charge model no clear trend can be observed for the charges of the deprotonated complexes.

3.3.1.2. Transition metal (II) complexes and selection of the proper charge model

The atomic partial charges for vacuum geometries of the transition metal (II) complexes generated in vacuum and implicit water are listed in Table A6 of the Appendix. Higher

polarity of the water ligands of protonated species under vacuum conditions compared to the implicit water is due to the smaller basis set used in the latter case. Partial charges of the oxygen atoms generated in vacuum conditions, based on the vacuum geometries of the protonated complexes involving Mn and Fe, are nearly identical for transition metal (III) complexes (Table A4, top part) and transition metal (II) complexes (Table A6, top part). The difference in the polarities of the water ligands is also not pronounced for transition metal (III) versus (II) complexes under vacuum conditions. This is not realistic, since the oxidized transition metal bearing larger positive charge and smaller radius should polarize water ligands stronger than the reduced transition metal. This artifact is also obtained comparing polarities of ligands for the protonated species of transition metal (III) [Table A4, bottom part] versus transition metal (II) complexes (Table A6, bottom part) of Mn and Fe generated in dielectric medium ($\varepsilon = 80$). This may be related to the so-called electron leakage phenomenon being stronger for the transition metal (II) complexes, which carry more electron density in the valence shell (Schmidt am Busch and Knapp 2004). The most promising combination in this comparison is when for the transition metal (III) complexes the geometry is optimized in vacuum and the partial charges are also generated in vacuum ($\varepsilon = 1$), while for the transition metal (II) complexes they are obtained in presence of implicit water ($\varepsilon = 80$). Corresponding charges are listed in the top part of Table A4 and in the bottom part of the Table A6 of the Appendix, respectively. Identical results are also obtained for QM/MM geometries (Table A7).

### 3.3.2. Stable spin state of the hexa-aqua transition metal complexes

An approximate half and half distribution of high and low spin states of a transition metal complex, known as spin crossover phenomenon, occurs if the energy difference between two spin states is in the range of RT, which is 0.59 kcal·mol^{-1} for ambient temperature. In case of larger energy differences molecules exist predominantly in one of the possible spin states. The stable spin configurations of all considered protonated complexes are listed in Table 1. All complexes considered in this study, with exception of the hexa-aqua Co(III) complex, retained their stable spin state upon deprotonation. There is some discrepancy in the literature regarding the stable spin state of the deprotonated hexa-

aqua Co(III) complex. Using a reaction field energy approach for vacuum geometries, 1.2 kcal·mol^{-1} difference was found in favor of the high spin state (Gilson and Durrant 2009). In more recent work using reaction field geometries with a larger basis set the low spin state was found to be more stable (Jerome, Hughes et al. 2014). The evaluation of relative gas-phase electronic energy difference between protonated (which has low spin closed shell electron configuration) and deprotonated (which has high spin open shell electron configuration) hexa-aqua Co(III) complex, depends on the choice of DFT formalism describing the open shell species. It is not quite clear, which formalism was used to describe the deprotonated high-spin state of this complex in recent works (Gilson and Durrant 2009, Jerome, Hughes et al. 2014). Therefore, in this work both spin states for this complex were carefully considered employing basis set of even higher precision (as described before) and different DFT formalisms (for the high spin case) to evaluate the ground state electronic energies.

Using the open shell restricted versus unrestricted formalism for computation of the electronic energy of the high spin deprotonated hexa-aqua Co(III) complex leads to 3.9 kcal·mol^{-1} difference (see Table A8 in the Appendix). Such large discrepancy indicates the presence of different types of systematic errors in these two approaches. Based on the agreement between our computed and measured pK$_A$ values, it appears that using the unrestricted open shell formalism leads to an over-stabilization of the deprotonated relative to the protonated state. Such behavior is generally expected due to spin-contamination present in the unrestricted open shell formalism. However, based on the expectation value of the total spin operator S^2 (Table A9), the spin-contamination was negligible in this case. Hence, the computation of accurate relative electronic energies between closed and open shell molecular systems is hampered, when restricted and unrestricted DFT formalisms are used in a mixed manner.

Appropriate relative energies between protonated and deprotonated hexa-aqua Co(III) complex evaluated based on the restricted DFT formalism are shown in Table A10 of the Appendix. Accordingly, for the Co(III) complex with geometry optimized in vacuum, the high spin configuration of the deprotonated species is clearly favored in vacuum by 15.9 kcal·mol^{-1} (Table A10). On the other hand, the solvation energy for the low spin configuration of this complex in water is larger by 15.0 kcal·mol^{-1}, as compared to the high

spin configuration, such that in aqueous solution the high spin deprotonated hexa-aqua Co(III) complex is still favored but by only 0.9 kcal·mol^{-1} (Table A10). Hence, a spin state change according to ($t_{2g}^6 e_g^0 \rightarrow t_{2g}^4 e_g^2$) may occur upon deprotonation of this complex in water. Corresponding geometries for the high and low spin configurations of deprotonated hexa-aqua Co(III) complex are shown in Figs. 6a and 6b, respectively. Estimating this energy difference with QM/MM geometries (2.3 kcal·mol^{-1}) favors the high spin state even more, as shown in Table A10 of the Appendix. Nevertheless, these energies may contain systematic errors, such that we cannot make a clear decision about the nature of the spin state of the deprotonated hexa-aqua Co(III) complex in water. In particular the 0.9 kcal·mol^{-1} energy difference, found based on the vacuum geometries, is too close to the value of RT (0.59 kcal·mol^{-1}), suggesting that this complex may well be a subject of spin crossover. Therefore, pK$_A$ values for both spin states of this complex are computed.
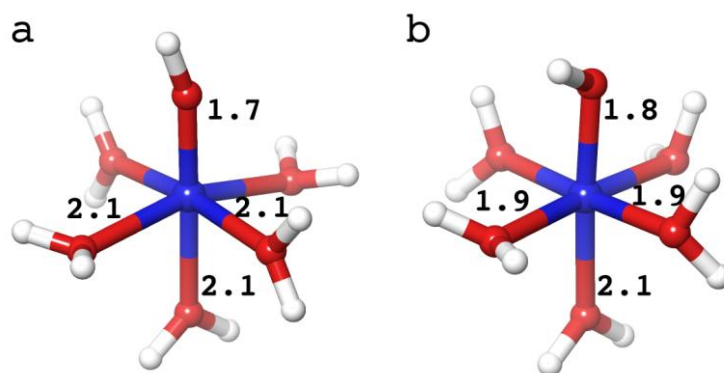

Figure 6. Geometries of the deprotonated hexa-aqua Co(III) complex obtained in vacuum for **a)** high and **b)** low spin configuration. Bond lengths for axial and equatorial ligands are given in [Å].

The resulting pK$_A$ values for vacuum and QM/MM geometries are 2.7 and 3.4 for low spin (no spin state change) and 2.0 and 1.7, respectively, if the spin state change is considered, both in reasonable agreement with the measured value 2.9 (Gilson and Durrant 2009) [Table A11].

3.3.3. Jahn-Teller effect in hexa-aqua transition metal complexes

Geometries of the complexes $[Ti(H_2O)_6]^{3+}$, $[V(H_2O)_6]^{3+}$ and $[Ru(H_2O)_6]^{3+}$ obtained in vacuum or in presence of explicit water had distortions expected from the symmetry and conservation of energy, i.e. tetragonal compression for the $(t_{2g}^{1} e_g^{0})$ and elongation for the $(t_{2g}^{2} e_g^{0})$ and $(t_{2g}^{5} e_g^{0})$ configurations, according to Figs. A1, A2 and A5 of the Appendix, respectively. Interestingly, a tetragonal compression expected for the $(t_{2g}^{4} e_g^{2})$ configuration (Fig. A4) did not take place for the optimized geometries of the $[Fe(H_2O)_6]^{2+}$ complex. Instead all three bond pairs acquire slightly different lengths, indicating a more complex orbital splitting mechanism leading to the tetragonal elongation observed for this system. In all four cases however the JTE is small (Table 1), and need not to be discussed in more detail.

The JTE is significant for the hexa-aqua Mn(III) complex, which possesses a stable high spin configuration $(t_{2g}^{3} e_g^{1})$ (Table 1). Symmetric splitting of the e_g orbitals (Fig. A4) does not allow straightforward prediction of the type of distortion in this case, i.e. which of the $d_{x^2-y^2}$ and d_{z^2} orbitals will receive the electron. Computation of both possibilities yielded geometries shown in Figs. 7a and 7b. Thereby the geometry with tetragonal elongation is by 1.2 kcal·mol^{-1} (0.6 kcal·mol^{-1} due to gas phase energy, and 0.6 kcal·mol^{-1} due to solvation energy) more stable than the geometry with tetragonal compression (Table A12). This result agrees well with earlier computations [(Kallies and Meier 2001) and references therein].
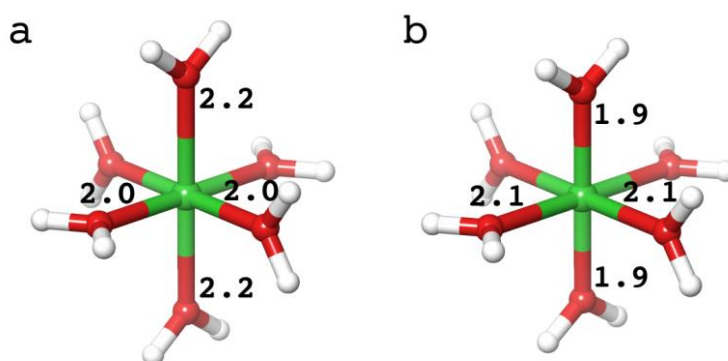
Figure 7. Two types of distorted geometries for the hexa-aqua Mn(III) complex obtained in vacuum are shown. **a)** elongated, and **b)** compressed. Bond lengths of axial and equatorial ligands are given in [Å].

3.3.4. Influence of basis sets on the gas phase energies

As it has been mentioned before, two basis sets cc−pVQZ(-g) (Dunning 1989) and cc−pVTZ (Dunning 1989, Kendall, Dunning et al. 1992, Woon and Dunning 1993, Woon and Dunning 1994) were applied to the ligand atoms to study the effect of basis set on computed electronic energies of hexa-aqua transition metal complexes. RMS deviations of the cc−pVTZ based gas phase basicities ΔG_g (eq. 4) from the more accurate cc−pVQZ(-g) based values are 0.7 and 0.8 kcal·mol^{-1} for vacuum and QM/MM geometry models, respectively (see Figs. A6a and A6b in the Appendix). Common trend of triple−ζ (cc−pVTZ) based relative energies to underestimate the quadruple−ζ [cc−pVQZ(-g)] based relative energies is in good agreement with other work (Schmidt am Busch and Knapp 2004). In this case the deviation seems to be related to the metal's electron configuration (Table 1). Such that, for the first row transition metal (III) complex geometries optimized in vacuum, the discrepancies between triple−ζ and quadruple−ζ based electronic energies are generally increasing with the occupation of d-orbitals (see Tables A10 and A13 of the Appendix). For Sc(III) in ($t_{2g}^{0} e_{g}^{0}$) configuration, the corresponding discrepancy is 0.3 kcal·mol^{-1}; from Ti(III) [$t_{2g}^{1} e_{g}^{0}$] over V(III) [$t_{2g}^{2} e_{g}^{0}$] to Cr(III) [$t_{2g}^{3} e_{g}^{0}$] the discrepancies increase from 0.6 to 0.7 kcal·mol^{-1}, till the t_{2g} sub-shell gets half-populated with electrons for Cr(III); for Mn(III) [$t_{2g}^{3} e_{g}^{1}$] and Fe(III) [$t_{2g}^{3} e_{g}^{2}$], which possess unpaired electrons in e_g sub-shell the discrepancies reach its maximum value of 1.0 kcal·mol^{-1}. For Co(III) [$t_{2g}^{6} e_{g}^{0}$] it drops back to 0.7 kcal·mol^{-1}, assuming no spin state change upon deprotonation. If a spin state change ($t_{2g}^{6} e_{g}^{0} \rightarrow t_{2g}^{4} e_{g}^{2}$) is considered, the discrepancies between triple−ζ and quadruple−ζ based electronic energies are −0.3 and 0.7 kcal·mol^{-1} for the restricted open shell and unrestricted DFTs, respectively. However, for the second row transition metal complexes with Ru(III) [$t_{2g}^{5} e_{g}^{0}$] and Rh(III) [$t_{2g}^{6} e_{g}^{0}$] geometry optimized in vacuum the deviation is negligible (0.1 kcal·mol^{-1}). And for the first row transition metal (II) complexes no clear trend can be observed (approximated geometries with bond angles constraints were used for the deprotonated species of these complexes). Thus, the maximum deviation of triple−ζ from quadruple−ζ based electronic energies of −1.6 kcal·mol^{-1} is obtained for Zn(II) [$t_{2g}^{6} e_{g}^{4}$] with filled d-shell, followed by Mn(II) [$t_{2g}^{3} e_{g}^{2}$] with half filled d-shell (−0.6 kcal·mol^{-1}), then Fe(II)

[t_{2g}^4 e_g^2, -0.3 kcal·mol^{-1}] and Ni(II) [t_{2g}^6 e_g^2, 0.1 kcal·mol^{-1}] with intermediate occupations of d-orbitals.

These trends apply to the QM/MM geometry models as well (Fig. A6b), except that here discrepancies between quadruple–ζ and triple–ζ based ΔG_g values for V(III), Ru(III) and Rh(III) increase to 0.9, 0.3 and 0.5 kcal·mol^{-1}, respectively; while it practically vanishes for Fe(II) (0.1 kcal·mol^{-1}). For Co(III) considering spin state change, deviations are increased to 1.2 and 1.1 kcal·mol^{-1}, for restricted open shell and unrestricted DFT, respectively (Tables A10 and A13 in the Appendix).

As it will be shown latter, for the majority of considered complexes, pK_A values computed with the quadruple–ζ basis set are shifted towards more acidic values compared to measured values. Hence, using a smaller basis set will increase that discrepancy. Therefore, triple–ζ basis set is not used in the following.

## 3.3.5. Comparison of energy terms computed based on vacuum versus QM/MM geometry models

The comparison of computed energy terms ΔG_g (eq. 4), $\Delta\Delta G_{solv}$ (eq. 7) and ΔG_{aq} (eq. 3) between vacuum and QM/MM geometry models is performed by considering the differences shown in eqs. 30-32 for all studied complexes.

$$\Delta(\Delta G_g) = \Delta G_g(vac) - \Delta G_g(QM/MM) \tag{30}$$

$$\Delta(\Delta\Delta G_{solv}) = \Delta\Delta G_{solv}(vac) - \Delta\Delta G_{solv}(QM/MM) \tag{31}$$

$$\Delta(\Delta G_{aq}) = \Delta G_{aq}(vac) - \Delta G_{aq}(QM/MM) \tag{32}$$

Corresponding results are shown in Fig. 8. The difference in gas phase basicities $\Delta(\Delta G_g)$ is positive everywhere (except for the hexa-aqua Mn(II) complex), and in the majority of cases it is larger in magnitude as compared to the difference in solvation energy term $\Delta(\Delta\Delta G_{solv})$. Exceptions are complexes of Fe(III), low spin Co(III), Mn(II) and Ni(II). Interestingly, the magnitudes of the differences $\Delta(\Delta G_g)$ and $\Delta(\Delta\Delta G_{solv})$ seem to be related to the valence electron configuration of the central metal ion (Table 1).
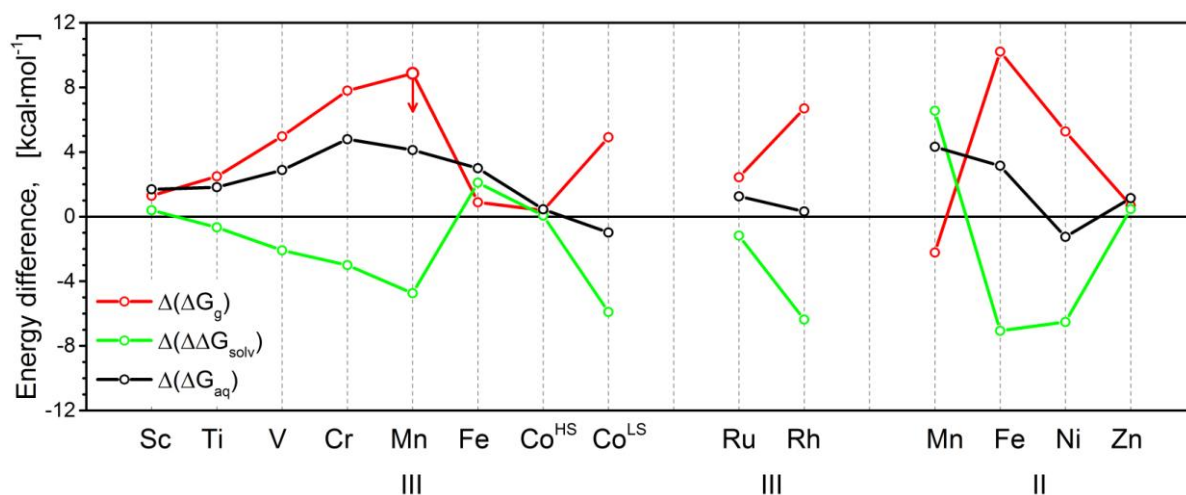
Figure 8. Difference in free energy terms $\Delta(\Delta G_g) = \Delta G_g(\text{vac}) - \Delta G_g(\text{QM/MM})$, $\Delta(\Delta\Delta G_{solv}) = \Delta\Delta G_{solv}(\text{vac}) - \Delta\Delta G_{solv}(\text{QM/MM})$, and $\Delta(\Delta G_{aq}) = \Delta G_{aq}(\text{vac}) - \Delta G_{aq}(\text{QM/MM})$, computed with molecular geometries optimized in vacuum or in presence of explicit water using QM/MM method for all transition metal (III) and (II) complexes studied in this work. Superscripts HS and LS denote the high and low spin states of the deprotonated hexa-aqua Co(III) complex, respectively.

3.3.5.1. Gas phase basicities

The magnitude of $\Delta(\Delta G_g)$ term increases step-by-step from Sc(III) $[t_{2g}^0 e_g^0]$ to Cr(III) $[t_{2g}^3 e_g^0]$ upon half filling of the t_{2g} sub-shell (Fig. 8). Then, it should decrease, as shown in the following, until half filling of the e_g sub-shell at Fe(III) $[t_{2g}^3 e_g^2]$. Note that the Mn(III) $[t_{2g}^3 e_g^1]$ departs from this pattern due to the incorrect order of protonated versus deprotonated energies predicted based on the QM/MM geometry model of the hexa-aqua Mn(III) complex. Gas phase basicity $\Delta G_g(\text{vac})$, computed based on the vacuum geometry model for this complex is 6.7 kcal·mol^{-1}, (Table. A10 in the Appendix), suggesting that the protonated species is more stable than the deprotonated species. The same energy term falsely receives a negative sign based on the QM/MM geometry model $\Delta G_g(\text{QM/MM}) = -2.2$ kcal·mol^{-1} (Table. A10). This assumption is based on the agreement between measured and computed pK_A values obtained for these two types of geometry models of the hexa-aqua Mn(III) complex (Table. A11 of the Appendix). Any positive $\Delta G_g(\text{QM/MM})$ value for this complex would lead to a $\Delta(\Delta G_g)$ value smaller than 6.7 kcal·mol^{-1} (Fig. 8), supporting the assumption, that $\Delta(\Delta G_g)$ should drop after Cr(III) at

Mn(III) and Fe(III). For the Co(III) complex the $\Delta(\Delta G_g)$ value is small if the change in spin state is taken into account (Table 1), otherwise it is larger than at Fe(III) [due to the empty e_g sub-shell in the low spin Co(III)]. For the hexa-aqua Ru(III) and Rh(III) complexes $\Delta(\Delta G_g)$ increases upon occupation of the t_{2g} sub-shell. For transition metal (II) complexes the trends are less clear due to the approximate geometries used in the vacuum geometry model. Therefore, no further comparisons are performed for the transition metal (II) complexes in the following.

Average lengths of all bond types for vacuum and QM/MM geometry models for all studied transition metal complexes are shown in Tables A2 and A3 of the Appendix, respectively.

3.3.5.2. Solvation energy differences

Trends found for the $\Delta(\Delta G_g)$ term are valid also for the $\Delta(\Delta\Delta G_{solv})$ difference, just with inverted order (Fig. 8). However some noise may be generally present here due to the conformational dependence of the numerical instabilities associated with the least-squares fitting of the ESP charges. Nevertheless the estimation of the associated rank deficiency was outside of the scope of this study. It is interesting to note, that also the value for the solvation energy term $\Delta(\Delta\Delta G_{solv})$ seems to depart from the pattern for the Mn(III) complex.

3.3.6. Charge distribution in transition metal (III) complexes based on the RESP charges

Charge distributions for the protonated (solid lines) and deprotonated (dashed lines) species of the first row transition metal (III) complexes computed in vacuum and in QM/MM geometry are shown in Figs. 9a and 9b, respectively. Main differences in the shapes of the charge distribution contours between these two geometry models appear for the protonated complexes with centers from Sc(III) to Cr(III) (solid lines), and for the deprotonated complexes with centers from Cr(III) to Co(III) (dashed lines). It deserves attention, that the RESP charge at the metal in the hexa-aqua Mn(III) complex with QM/MM geometry falsely remains identical in both protonation states. Comparison of vacuum versus QM/MM charge distributions for the second row transition metal complexes is less informative, due to availability of only two complexes (Figs. A7a and A7b). Nevertheless, on

these contours one can observe an extra stabilization of the π-donor OH-ligand at the Ru(III) center [$t_{2g}^5 e_g^0$], as compared to the Rh(III) center [$t_{2g}^6 e_g^0$] with full t_{2g} sub-shell. Overall, severe discrepancies in the charge distributions obtained with vacuum versus QM/MM geometry models just reflect the conformational dependence of the RESP procedure.
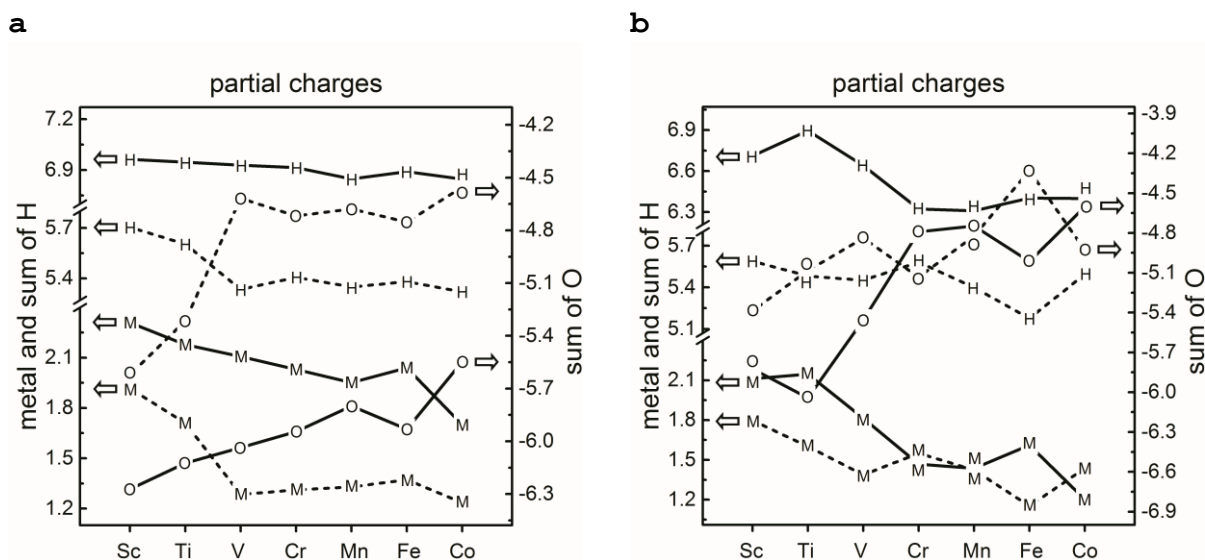

Figure 9. Partial charge of metal, net partial charges of hydrogen and oxygen atoms computed in vacuum for **a:** vacuum and **b:** QM/MM geometries of protonated (solid lines) and deprotonated (dashed lines) species of transition metal (III) complexes with metals belonging to the first transition series. The low spin deprotonated Co(III) complex is not shown for simplicity.

There is a linear correlation between RESP charges of the metal ions and measured electron affinities (EA) (Table A14) at least for the protonated transition metal (III) complexes involving metals from Sc(III) to Fe(III) whose geometry was optimized in vacuum (Fig. A8a of the Appendix). Interestingly, the correlation line intersects the ordinate axis at 3.31 charge units, meaning, that for a hypothetical system, with center possessing EA of 0 eV, a leakage of 0.31 electrons from the center will take place. This may well be due to numerical instabilities associated with the RESP procedure, resulting in over-polarization of the buried atoms. The partial charge of a metal ion, being buried by ligands, does not affect solvation energy directly. However, according to Fig. 9 the variation of the metal's charge from system to system is clearly reflected in the change of the net oxygen charge as well. Therefore, the latter too is in a linear relationship with the EA of the metal ion for the mentioned systems (Fig. A8b of the Appendix), such that (charge $= -7.60 - 0.05 \cdot$EA).

3.3.7. Computed pK$_A$ values

Computed pK$_A$ values are shown in Table A11 and Fig. 10. Excluding the outliers hexa-aqua Cr(III) with vacuum geometry and hexa-aqua Mn(III) with QM/MM geometry, the root mean square deviations (RMSD) between computed and measured pK$_A$ values are 1.2 and 1.0 pH units, respectively (Fig. 10). The severe underestimation of the measured pK$_A$ value by 4.1 pH units obtained for the Mn(III) complex with the QM/MM geometry is partially due to the falsely predicted energy order of protonated versus deprotonated species, namely $\Delta G_g = -2.2$ kcal·mol^{-1}. A positive ΔG_g would improve the computed pK$_A$ value by more than 2.2/1.365 = 1.6 pH units.
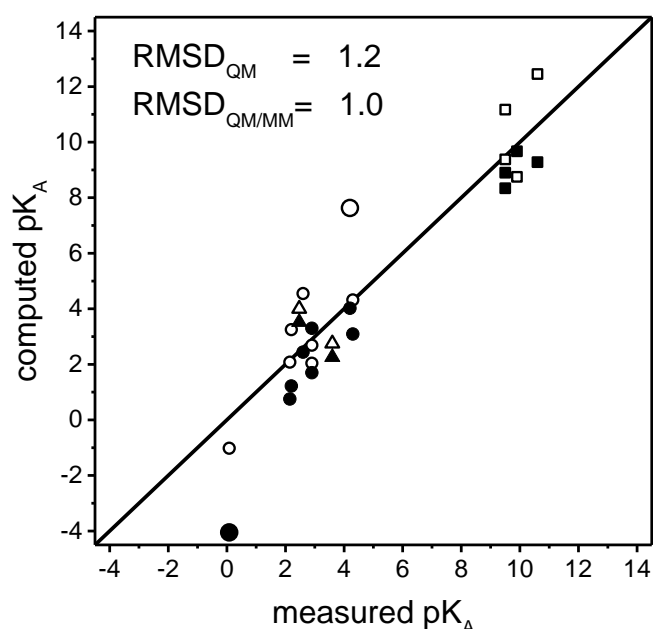
Figure 10. Correlation diagram of measured and computed pK$_A$ values for vacuum (QM) and QM/MM geometry models shown as open or closed symbols, respectively. Circles and triangles represent pK$_A$ values for the first- and second-row transition metal (III) complexes, respectively. While squares represent transition metal (II) complexes. Two outliers, corresponding to the complexes with Mn(III) (closed circle) and Cr(III) (open circle) are indicated by larger symbols. They are not included in the RMSD values, which are 1.0 and 1.2 pH units.

Another contribution to the discrepancy between computed and measured pK_A values may come from a wrong charge distribution obtained for the QM/MM geometry of the hexa-aqua Mn(III) complex. Overestimated pK_A values of the hexa-aqua Cr(III) [by 3.4 pH units], V(III) [by 2.0 pH units] and Ru(III) [by 2.0 pH units] complexes obtained with vacuum geometry may also be related to the seemingly wrong charge distribution of these complexes.

The overestimations of the measured pK_A values of the hexa-aqua Mn(II) and Fe(II) complexes with vacuum geometries by 1.9 and 1.7 pH units, respectively, may be rationalized by the approximate geometry used for the deprotonated species of these two transition metal (II) complexes.

QM/MM geometries yield generally more acidic pK_A values compared to the measured values, and pK_A values computed for vacuum geometries. The latter is due to smaller gas phase basicities computed with QM/MM geometries compared to the models in vacuum geometry (Fig. 8).

4. DISCUSSION

Accurate computation of tautomer equilibria of lactams with a robust DFT method is a challenging task, even under vacuum conditions. The selection of DFT functionals for benchmarking in this study was done based on previous work in (Piacenza and Grimme 2004). They showed, that using DFT functionals with a small amount of exact exchange term yields tautomerization energies systematically deviating from the reference energies computed with accurate QCISD(T) method, if tautomeric species possess different aromatic character. Thereby, in current work, the set of reference energies from (Piacenza and Grimme 2004) is extended in number and quality. The B3LYP functional with an exact exchange term of 20% is used in the present only to test the performance of the B3LYP-LOC empirical correction scheme, while all other considered density functionals possess a larger contribution of exact exchange, i.e. 28% for PW6B95, and 50% for BH&HLYP and BH&HLYP(G). Being superior to B3LYP, the B3LYP-LOC is found to be insufficiently good for the current application, perhaps since the set of LOC correction terms were fitted for a smaller basis set than cc−pVQZ used in current work. While larger contribution of exact exchange in BH&HLYP and BH&HLYP(G) DFT functionals makes them slightly superior in some cases, the PW6B95 DFT functional showed generally better performance in handling various types of molecules, including those with charges localized at certain parts of molecule (Fig. 3 of the publication "Computations of 36 tautomer/isomer equilibria of different lactams"). Thus, the PW6B95 DFT functional precisely reproduced the reference relative energy for isomer pair involving zwitterionic species (pair 15 in Fig. 3 of the tautomer article), while all other DFT methods failed for this task (with deviations of 2.0 kcal·mol^{-1} or more). Computation of transition states reveals too high activation barriers (about 70 kcal·mol^{-1}, Fig. S1 in the Supporting Information of the tautomer article) for the considered zwitterions, such that they hardly exist in vacuum at ambient temperature. However, the zwitterionic states exist in aqueous solution. For computation of the tautomer

pair energies for solvated structures involving zwitterions, which is performed using the thermodynamic cycle connecting gas and liquid phases, an accurate computation of these virtual pair energies in vacuum is required. The most challenging system for all considered DFT functionals appears to be amine-imine tautomer pair of cytosine (yielding deviations exceeding 1.0 kcal·mol^{-1}, with all methods used). This problem is however not connected to the particular amine-imine type of tautomerism, since for amine-imine tautomers of isocytosine all three density functionals yield satisfactory energetics. Due to large discrepancy between amine-imine tautomer pair energies for cytosine computed using PW6B95 DFT functional and reference QCISD(T)(q–ζ) method, this pair of tautomers is not considered when computing the deviation (of PW6B95 based tautomer pair energies from the QCISD(T) based reference energies) versus ΔNICS(1)$_{zz}$ correlation line (Fig. 4 of the tautomer article). The latter is used to construct the following post Hartree-Fock correction scheme, that in conjunction with B3LYP/6-31G** geometries and vibrational energies provides tautomerization or isomerization free energies for lactams with 0.5 kcal·mol^{-1} RMS deviation from the measured or computed reference energies obtained with QCISD(T)(q–ζ) method.

$$\Delta E^{(V/W)}(\text{PW6B95-corr}) = \Delta E^{(V/W)}(\text{PW6B95}) + 0.03 \cdot \Delta \text{NICS}(1)_{zz} \text{ kcal·mol}^{-1}, \qquad (33)$$

where $\Delta E^{(V/W)}$ denotes ground state electronic energy difference between tautomer/isomer species V and W.

Computation of aqueous pK_A values deals with the following complex issues, related to gas phase and solvation energy terms. (i) Computation of gas phase basicities for the molecules possessing closed versus open shell electron configurations in different protonation states shows high sensitivity to the DFT formalism (restricted or unrestricted) used for the treatment of the open shell systems. In the case of the hexa-aqua Co(III) complex, the usage of the unrestricted DFT formalism strongly overestimates the stability of the high spin deprotonated species, as compared to the restricted open shell DFT formalism. While the usage of unrestricted versus unrestricted and restricted versus restricted DFT formalisms is perfectly appropriate, the mixing of these two formalisms may yield dramatic discrepancies for relative energies. (ii) In some cases, such as transition metal (II) complexes studied in this work, the geometries of molecules strongly differ in gas and in solvent phases. In such situations the results become very sensitive to the selection of the

geometry, taking into account that the thermodynamic cycle assumes the same geometry for both phases. (iii) Another factor influencing gas phase energies is the choice of the basis set. Comparison of the triple–ζ and quadruple–ζ based gas phase basicities for the studied complexes reveals, that the corresponding discrepancy is related to the number and type of unpaired electrons in metal's valence shell. Thus, the discrepancy between triple–ζ and quadruple–ζ based gas phase basicities increases with the occupation number and most relevantly the energy of the occupied orbitals. It reaches its maximum for Mn(III) and Fe(III) possessing unpaired electrons in both the t_{2g} and e_g orbitals. Therefore, using high quality basis set is important for the computation of accurate pK_A values for complexes especially involving Mn(III) and Fe(III) ions. This conclusion will most likely also apply to multi-core transition metal complexes, and may be most relevant for such challenging systems as the manganese cluster enzyme in photosystem II. Larger basis sets were not tested in the present study, since they are not available in the software used. (iv) Atomic partial charges, used in electrostatic solvation energy computations, are very sensitive to the quality of the electrostatic potentials. The electron leakage artifact may influence the accuracy of the electrostatic potential to different extent dependent on the total charge of considered molecular system, thereby leading often to unphysical results. For this reason two different charge models had to be used for the transition metal (III) and (II) complexes, generated from electrostatic potentials computed (i) at vacuum conditions and (ii) in presence of implicit solvent. This helped to avoid inconsistencies with the physical picture regarding the polarity of ligands in the transition metal (III) versus (II) complexes. (v) The limitations of the RESP procedure used for the charge derivation also influence the computed solvation energies. Reflections of both, statistically poor determination of the charges of buried atoms, and the conformational dependence of RESP, are seen in the strange intersecting of the correlation line of metal's partial charge versus the EA value, and in the comparison of vacuum versus QM/MM geometry models, respectively. Considering the above mentioned problems, the procedure for pK_A computation suggested in this study works amazingly well, reproducing the measured pK_A values with the RMS deviation of about 1 pH units for each considered geometry model.

S U M M A R Y

In this PhD work appropriate procedures for computation of gas phase tautomer/isomer equilibria for lactams, involving amide-imidic acid and amine-imine tautomerisms; as well as aqueous acid dissociation constants for hexa-aqua complexes of transition metals belonging to the first and second transition series are elaborated.

The former procedure allows to reproduce available measured tautomer/isomer pair energies, as well as reference values computed using the CPU time demanding QCISD(T) method (with RMS deviation equal to 0.5 kcal·mol^{-1}) with considerably less CPU time. Gas phase energies computed with such accuracy in combination with solvation electrostatic energy computations will allow accurate prediction of tautomer/isomer equilibria in solvent environments, which has both fundamental and practical use as has been described before.

The procedure for pK_A computations allows reproduction of the available measured values for the challenging hexa-aqua transition metal complexes with RMS deviation equal to 1 pH units. Methodological experience and knowledge obtain with this prototypic systems will be applicable to multinuclear transition metal complexes involving titratable oxygens as well. Therefore, this work is an excellent starting point for the prediction of protonation states of OEC Mn$_4$Ca-cluster in PSII, which has both fundamental and technological importance.

ZUSAMMENFASSUNG

In dieser Doktorarbeit wurden Verfahren entwickelt zur präzisen Berechnung von i) Tautomer/Isomer Gleichgewichten von Lactams in der Gas-Phase (amide-imidic acid and amine-imine tautomerisms); und ii) Wasser-Dissoziationskonstanten von Hexaaquakomplexen der Übergangsmetallionen der ersten und zweiten Reihe.

Das erste Verfahren berechnet die Energien für Tautomer/Isomer Paare mit geringer Abweichung von 0.5 kcal/mol (RMSD) im Vergleich zu den experimentellen Messwerten und zu den Referenzwerten, die mit der aufwendigen QCISD(T)-Methode berechnet wurden. Kombiniert mit einer Berechnung der elektrostatischen Solvatationsenergie erlaubt das Verfahren präzise Vorhersagen von Tautomer/Isomer Gleichgewichten in den Lösung. Solche Vorhersagen sind von großem grundlegenden und praktischen Nutzen.

Das zweite Verfahren erlaubt die Berechnung von pKa Werten der Hexaaquakomplexe von Übergangsmetalionen mit einer Genauigkeit von 1pH (RMS) Einheiten. Die Erfahrung und Kentnisse, die mit diesen Prototyp-Systemen gewonnen wurden, können auf komplexere Systeme angewandt werden, wie z.B. multinukleare Übergangsmetallkomplexe mit titrierbaren Sauerstoff-Atomen. Diese Arbeit ist deshalb ein guter Startpunkt, um zuverlässige Vorhersagen der Protonierungszustände des OEC Mn4Ca-cluster in PSII zu erhalten, was von grosser Bedeutung ist.

A D D I T I O N A L   P U B L I C A T I O N S

Two-photon-induced singlet fission in rubrene single crystal

Authors: Ma L., Galstyan G., Zhang K.K., Kloc C., Sun H.D., Soci C., Michel-Beyerle M.E., Gurzadyan G.G.

Contribution:

- All quantum chemical computations
- Preparation of the parts of the manuscript related to the quantum chemical computations

Exploring the possible role of Glu286 in CcO by electrostatic energy computations combined with molecular dynamics

Authors: Woelke A.L., Galstyan G., Galstyan A., Meyer T., Heberle J., Knapp E.W.

Contribution:

- All quantum chemical computations
- Preparation of the parts of the manuscript related to the quantum chemical computations

Understanding selectin counter-receptor binding from electrostatic energy computations and experimental binding studies

Authors: Woelke A.L., Kuehne C., Meyer T., Galstyan G., Dernedde J., Knapp E.W.

Bibliography: Journal of Physical Chemistry B 117: 16443-16454, 2013

Contribution:

- All quantum chemical computations
- Preparation of the parts of the manuscript related to the quantum chemical computations

Lysine 362 in cytochrome c oxidase regulates opening of the K-channel via changes in pK_A and conformation

Authors: Woelke A.L., Galstyan G., Knapp E.W.

Contribution:

- All quantum chemical computations
- Preparation of the parts of the manuscript related to the quantum chemical computations

REFERENCES

Banks, J. L., H. S. Beard, Y. X. Cao, A. E. Cho, W. Damm, R. Farid, A. K. Felts, T. A. Halgren, D. T. Mainz, J. R. Maple, R. Murphy, D. M. Philipp, M. P. Repasky, L. Y. Zhang, B. J. Berne, R. A. Friesner, E. Gallicchio and R. M. Levy (2005). "Integrated modeling program, applied chemical theory (IMPACT)." *Journal of Computational Chemistry* **26**(16): 1752-1780.

Bashford, D., D. A. Case, C. Dalvit, L. Tennant and P. E. Wright (1993). "Electrostatic calculations of side-chain pK(a) values in myoglobin and comparison with NMR data for histidines." *Biochemistry* **32**(31): 8045-8056.

Bashford, D. and K. Gerwert (1992). "Electrostatic calculations of the pKa values of ionizable groups in bacteriorhodopsin." *Journal of Molecular Biology* **224**(2): 473-486.

Bayly, C. I., P. Cieplak, W. D. Cornell and P. A. Kollman (1993). "A well-behaved electrostatic potential based method using charge restraints for deriving atomic charges: the RESP model." *Journal of Physical Chemistry* **97**(40): 10269-10280.

Becke, A. D. (1993a). "Density-functional thermochemistry. III. The role of exact exchange." *Journal of Chemical Physics* **98**(7): 5648-5652.

Becke, A. D. (1993b). "A new mixing of Hartree-Fock and local density-functional theories." *Journal of Chemical Physics* **98**(2): 1372-1377.

Binkley, J. S. and J. A. Pople (1977). "Self-consistent molecular orbital methods. XIX. Split-valence Gaussian-type basis sets for beryllium." *Journal of Chemical Physics* **66**(2): 879-880.

Bochevarov, A. D., E. Harder, T. F. Hughes, J. R. Greenwood, D. A. Braden, D. M. Philipp, D. Rinaldo, M. D. Halls, J. Zhang and R. A. Friesner (2013). "Jaguar: A high-performance quantum chemistry software program with strengths in life and materials sciences." *International Journal of Quantum Chemistry* **113**(18): 2110-2142.

Clark, T., J. Chandrasekhar, G. W. Spitznagel and P. V. Schleyer (1983). "Efficient diffuse function-augmented basis sets for anion calculations. III. The 3-21+G basis set for first-row elements, Li-F." *Journal of Computational Chemistry* **4**(3): 294-301.

Corminboeuf, C., T. Heine, G. Seifert, P. V. Schleyer and J. Weber (2004). "Induced magnetic fields in aromatic [n]-annulenes − interpretation of NICS tensor components." *Physical Chemistry Chemical Physics* **6**(2): 273-276.

Cornell, W. D., P. Cieplak, C. I. Bayly and P. A. Kollman (1993). "Application of RESP charges to calculate conformational energies, hydrogen-bond energies, and free energies of solvation." *Journal of the American Chemical Society* **115**(21): 9620-9631.

Cox, N., D. A. Pantazis, F. Neese and W. Lubitz (2013). "Biological water oxidation." *Accounts of Chemical Research* **46**(7): 1588-1596.

Debye, P. and E. Hückel (1923). "Zur Theorie der Elektrolyte. I. Gefrierpunktserniedrigung und verwandte Erscheinungen." *Physikalische Zeitschrift* **24**(9): 185-206.

Ditchfie, R., W. J. Hehre and J. A. Pople (1971). "Self-consistent molecular-orbital methods. IX. Extended Gaussian-type basis for molecular-orbital studies of organic molecules." *Journal of Chemical Physics* **54**(2): 724-728.

Dunning, T. H. (1989). "Gaussian basis sets for use in correlated molecular calculations. I. The atoms boron through neon and hydrogen." *Journal of Chemical Physics* **90**(2): 1007-1023.

Fallah-Bagher-Shaidaei, H., C. S. Wannere, C. Corminboeuf, R. Puchta and P. V. Schleyer (2006). "Which NICS aromaticity index for planar π rings is best?" *Organic Letters* **8**(5): 863-866.

Francl, M. M., W. J. Pietro, W. J. Hehre, J. S. Binkley, M. S. Gordon, D. J. Defrees and J. A. Pople (1982). "Self-consistent molecular orbital methods. XXIII. A polarization-type basis set for second-row elements." *Journal of Chemical Physics* **77**(7): 3654-3665.

Friesner, R. A., E. H. Knoll and Y. Cao (2006). "A localized orbital analysis of the thermochemical errors in hybrid density functional theory: achieving chemical accuracy via a simple empirical correction scheme." *Journal of Chemical Physics* **125**(12): 124107/1-124107/24.

Frisch, M. J., J. A. Pople and J. S. Binkley (1984). "Self-consistent molecular orbital methods. 25. Supplementary functions for Gaussian basis sets." *Journal of Chemical Physics* **80**(7): 3265-3269.

Frisch, M. J., G. W. Trucks, H. B. Schlegel, G. E. Scuseria, M. A. Robb, J. R. Cheeseman, G. Scalmani, V. Barone, B. Mennucci, G. A. Petersson, H. Nakatsuji, M. Caricato, X. Li, H. P. Hratchian, A. F. Izmaylov, J. Bloino, G. Zheng, J. L. Sonnenberg, M. Hada, M. Ehara, K. Toyota, R. Fukuda, J. Hasegawa, M. Ishida, T. Nakajima, Y. Honda, O. Kitao, H. Nakai, T. Vreven, J. A. Montgomery, Jr., J. E. Peralta, F. Ogliaro, M. Bearpark, J. J. Heyd, E. Brothers, K. N. Kudin, V. N. Staroverov, R. Kobayashi, J. Normand, K. Raghavachari, A. Rendell, J. C. Burant, S. S. Iyengar, J. Tomasi, M. Cossi, N. Rega, J. M. Millam, M. Klene, J. E. Knox, J. B. Cross, V. Bakken, C. Adamo, J. Jaramillo, R. Gomperts, R. E. Stratmann, O. Yazyev, A. J. Austin, R. Cammi, C. Pomelli, J. W. Ochterski, R. L. Martin, K. Morokuma, V. G. Zakrzewski, G. A. Voth, P. Salvador, J. J. Dannenberg, S. Dapprich, A. D. Daniels, O. Farkas, J. B. Foresman, J. V. Ortiz, J. Cioslowski, and D. J. Fox (2009). Gaussian 09, revision A.02, Gaussian, Inc., Wallingford, CT.

Galstyan, A. and E. W. Knapp (2009). "Accurate redox potentials of mononuclear iron, manganese, and nickel model complexes." *Journal of Computational Chemistry* **30**(2): 203-211.

Gerega, A., L. Lapinski, M. J. Nowak, A. Furmanchuk and J. Leszczynski (2007). "Systematic effect of benzo-annelation on oxo-hydroxy tautomerism of heterocyclic compounds. Experimental matrix-isolation and theoretical study." *Journal of Physical Chemistry A* **111**(23): 4934-4943.

Gilson, R. and M. C. Durrant (2009). "Estimation of the pKa values of water ligands in transition metal complexes using density functional theory with polarized continuum model solvent corrections." *Dalton Transactions* (46): 10223-10230.

Goldfeld, D. A., A. D. Bochevarov and R. A. Friesner (2008). "Localized orbital corrections applied to thermochemical errors in density functional theory: The role of basis set and application to molecular reactions." *Journal of Chemical Physics* **129**(21), 214105/1-214105/13.

Grimme, S. (2003). "Improved second-order Moller-Plesset perturbation theory by separate scaling of parallel- and antiparallel-spin pair correlation energies." *Journal of Chemical Physics* **118**(20): 9095-9102.

Harihara, P. C. and J. A. Pople (1973). "The influence of polarization functions on molecular orbital hydrogenation energies." *Theoretica Chimica Acta* **28**(3): 213-222.

Hay, P. J. and W. R. Wadt (1985a). "Ab initio effective core potentials for molecular calculations. Potentials for K to Au including the outermost core orbitals." *Journal of Chemical Physics* **82**(1): 299-310.

Hay, P. J. and W. R. Wadt (1985b). "Ab initio effective core potentials for molecular calculations. Potentials for the transition metal atoms Sc to Hg." *Journal of Chemical Physics* **82**(1): 270-283.

Hehre, W. J., R. Ditchfie and J. A. Pople (1972). "Self-consistent molecular orbital methods. XII. Further extensions of Gaussian-type basis sets for use in molecular orbital studies of organic molecules." *Journal of Chemical Physics* **56**(5): 2257-2261.

Hehre, W. J. and J. A. Pople (1972). "Self-consistent molecular orbital methods. XIII. An extended Gaussian-type basis for boron." *Journal of Chemical Physics* **56**(8): 4233-4234.

Jahn, H. A. and E. Teller (1937). "Stability of polyatomic molecules in degenerate electronic states. I. Orbital degeneracy." *Proceedings of the Royal Society A* **161**(905): 220-235.

Jerome, S. V., T. F. Hughes and R. A. Friesner (2014). "Accurate pKa prediction in first-row hexaaqua transition metal complexes using the B3LYP-DBLOC method." *Journal of Physical Chemistry B* **118**(28): 8008-8016.

Jorgensen, W. L., J. Chandrasekhar, J. D. Madura, R. W. Impey and M. L. Klein (1983). "Comparison of simple potential functions for simulating liquid water." *Journal of Chemical Physics* **79**(2): 926-935.

Jorgensen, W. L., D. S. Maxwell and J. Tirado-Rives (1996). "Development and testing of the OPLS all-atom force field on conformational energetics and properties of organic liquids." *Journal of the American Chemical Society* **118**(45): 11225-11236.

Kallies, B. and R. Meier (2001). "Electronic structure of 3d $[M(H_2O)_6]^{3+}$ ions from Sc^{III} to Fe^{III}: A quantum mechanical study based on DFT computations and natural bond orbital analyses." *Inorganic Chemistry* **40**(13): 3101-3112.

Kaminski, G. A., R. A. Friesner, J. Tirado-Rives and W. L. Jorgensen (2001). "Evaluation and reparametrization of the OPLS-AA force field for proteins via comparison with accurate quantum chemical calculations on peptides." *Journal of Physical Chemistry B* **105**(28): 6474-6487.

Katritzky, A. R., C. D. Hall, B. El-Dien, M. El-Gendy and B. Draghici (2010). "Tautomerism in drug discovery." *Journal of Computer-Aided Molecular Design* **24**(6-7): 475-484.

Kendall, R. A., T. H. Dunning and R. J. Harrison (1992). "Electron affinities of the first-row atoms revisited. Systematic basis-sets and wave functions." *Journal of Chemical Physics* **96**(9): 6796-6806.

Knoll, E. H. and R. A. Friesner (2006). "Localized orbital corrections for the calculation of ionization potentials and electron affinities in density functional theory." *Journal of Physical Chemistry B* **110**(38): 18787-18802.

Koch, W. and M. C. Holthausen (2000). A chemist's guide to density functional theory. Weinheim, Wiley-VCH.

Krishnan, R., J. S. Binkley, R. Seeger and J. A. Pople (1980). "Self-consistent molecular orbital methods .XX. A basis set for correlated wave functions." *Journal of Chemical Physics* **72**(1): 650-654.

Lee, B. and F. M. Richards (1971). "The interpretation of protein structures: Estimation of static accessibility." *Journal of Molecular Biology* **55**(3): 379-400.

Lee, C. T., W. T. Yang and R. G. Parr (1988). "Development of the Colle-Salvetti correlation-energy formula into a functional of the electron density." *Physical Review B* **37**(2): 785-789.

Leslie, M. (2009). "On the origin of photosynthesis." *Science* **323**(5919): 1286-1287.

Martin, Y. C. (2009). "Let's not forget tautomers." *Journal of Computer-Aided Molecular Design* **23**(10): 693-704.

McLean, A. D. and G. S. Chandler (1980). "Contracted Gaussian basis sets for molecular calculations. I. Second row atoms, Z=11-18." *Journal of Chemical Physics* **72**(10): 5639-5648.

McQuarrie, D. A. (2000). Statistical mechanics. Sausalito, CA, University Science Books.

Milletti, F. and A. Vulpetti (2010). "Tautomer preference in PDB complexes and its impact on structure-based drug discovery." *Journal of Chemical Information and Modeling* **50**(6): 1062-1074.

Mohr, P. J., B. N. Taylor and D. B. Newell (2012). "CODATA Recommended values of the fundamental physical constants: 2010." *Journal of Physical and Chemical Reference Data* **41**(4): 043109/1-043109/84.

Parr, R. G. and W. Yang (1989). Density-functional theory of atoms and molecules. New York, NY, Oxford University Press.

Perdew, J. P., J. A. Chevary, S. H. Vosko, K. A. Jackson, M. R. Pederson, D. J. Singh and C. Fiolhais (1992). "Atoms, molecules, solids, and surfaces: Applications of the generalized gradient approximation for exchange and correlation." *Physical Review B* **46**(11): 6671-6687.

Perdew, J. P., J. A. Chevary, S. H. Vosko, K. A. Jackson, M. R. Pederson, D. J. Singh and C. Fiolhais (1993). "Erratum: Atoms, molecules, solids, and surfaces: Applications of the generalized gradient approximation for exchange and correlation (Vol 46, Pg 6671, 1992)." *Physical Review B* **48**(7): 4978-4978.

Persson, I. (2010). "Hydrated metal ions in aqueous solution: How regular are their structures?" *Pure and Applied Chemistry* **82**(10): 1901-1917.

Piacenza, M. and S. Grimme (2004). "Systematic quantum chemical study of DNA-base tautomers." *Journal of Computational Chemistry* **25**(1): 83-99.

Pople, J. A., M. Head-Gordon and K. Raghavachari (1987). "Quadratic configuration interaction. A general technique for determining electron correlation energies." *Journal of Chemical Physics* **87**(10): 5968-5975.

Pospisil, P., P. Ballmer, L. Scapozza and G. Folkers (2003). "Tautomerism in computer-aided drug design." *Journal of Receptors and Signal Transduction* **23**(4): 361-371.

Robertazzi, A., A. Galstyan and E. W. Knapp (2014). "PSII manganese cluster: Protonation of W2, O5, O4 and His337 in the S1 state explored by combined quantum chemical and electrostatic energy computations." *Biochimica et Biophysica Acta – Bioenergetics* **1837**(8): 1316-1321.

Schleyer, P. V., C. Maerker, A. Dransfeld, H. J. Jiao and N. J. R. V. Hommes (1996). "Nucleus-independent chemical shifts: A simple and efficient aromaticity probe." *Journal of the American Chemical Society* **118**(26): 6317-6318.

Schmidt am Busch, M. and E. W. Knapp (2004). "Accurate pKa determination for a heterogeneous group of organic molecules." *Europenan Journal of Chemical Physics and Physical Chemistry* **5**(10): 1513-1522.

Schmidt Am Busch, M. and E. W. Knapp (2005). "One-electron reduction potential for oxygen- and sulfur-centered organic radicals in protic and aprotic solvents." *Journal of the American Chemical Society* **127**(45): 15730-15737.

Schrödinger, LLC (2010). Jaguar, version 7.7, New York, NY.

Schrödinger, LLC (2014a). Jaguar, version 8.3, New York, NY.

Schrödinger, LLC (2014b). Impact, version 6.2, New York, NY.

Singh, U. C. and P. A. Kollman (1984). "An approach to computing electrostatic charges for molecules." *Journal of Computational Chemistry* **5**(2): 129-145.

Steiner, E., P. W. Fowler and L. W. Jenneskens (2001). "Counter-rotating ring currents in coronene and corannulene." *Angewandte Chemie - International Edition* **40**(2): 362-366.

Stephens, P. J., F. J. Devlin, C. F. Chabalowski and M. J. Frisch (1994). "Ab initio calculation of vibrational absorption and circular dichroism spectra using density functional force fields." *Journal of Physical Chemistry* **98**(45): 11623-11627.

Umena, Y., K. Kawakami, J. R. Shen and N. Kamiya (2011). "Crystal structure of oxygen-evolving photosystem II at a resolution of 1.9Å." *Nature* **473**(7345): 55-60.

Vosko, S. H., L. Wilk and M. Nusair (1980). "Accurate spin-dependent electron liquid correlation energies for local spin density calculations: a critical analysis." *Canadian Journal of Physics* **58**(8): 1200-1211.

Warshel, A. and M. Levitt (1976). "Theoretical studies of enzymic reactions: Dielectric, electrostatic and steric stabilization of carbonium ion in reaction of lysozyme." *Journal of Molecular Biology* **103**(2): 227-249.

Wolinski, K., J. F. Hinton and P. Pulay (1990). "Efficient implementation of the gauge-independent atomic orbital method for NMR chemical shift calculations." *Journal of the American Chemical Society* **112**(23): 8251-8260.

Woon, D. E. and T. H. Dunning (1993). "Gaussian basis sets for use in correlated molecular calculations. III. The atoms aluminum through argon." *Journal of Chemical Physics* **98**(2): 1358-1371.

Woon, D. E. and T. H. Dunning (1994). "Gaussian basis sets for use in correlated molecular calculations. IV. Calculation of static electrical response properties." *Journal of Chemical Physics* **100**(4): 2975-2988.

Zhao, Y. and D. G. Truhlar (2005). "Design of density functionals that are broadly accurate for thermochemistry, thermochemical kinetics, and nonbonded interactions." *Journal of Physical Chemistry A* **109**(25): 5656-5667.

A P P E N D I X
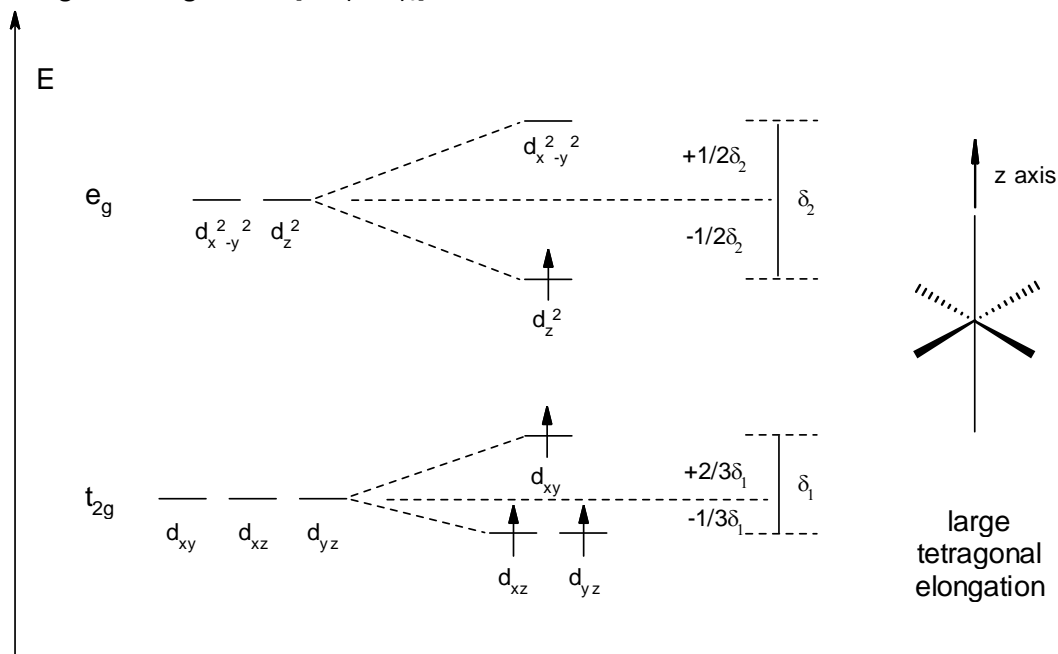
Appendix includes the following material:

Figure A1. Jahn-Teller effect for $t_{2g}^1 e_g^0$ configuration leads to small tetragonal compression
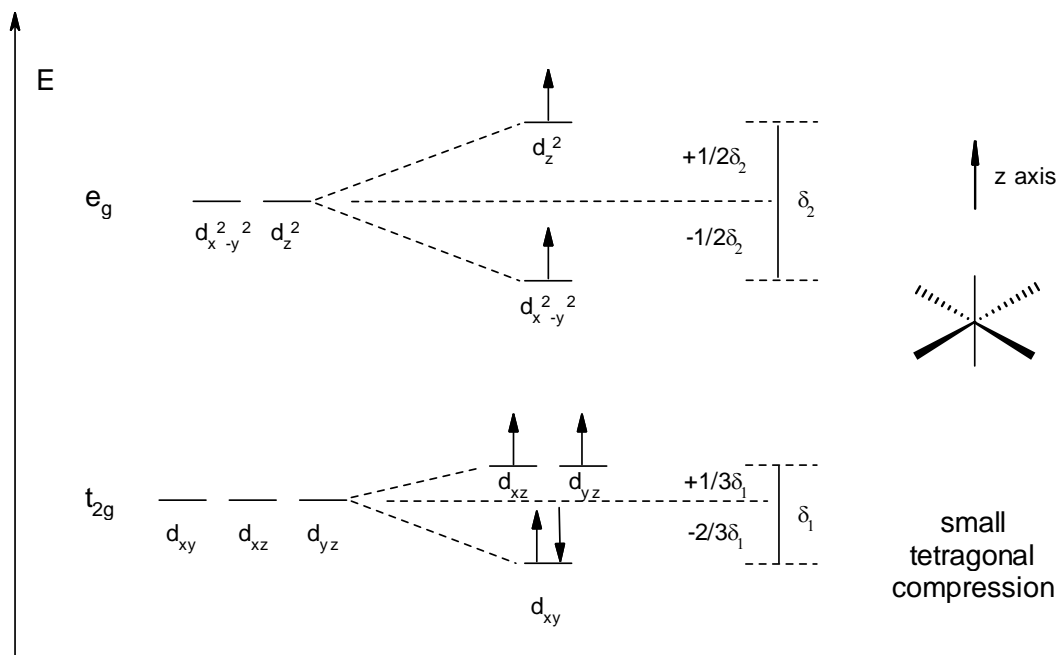

Figure A2. Jahn-Teller effect for $t_{2g}^2 e_g^0$ configuration leads to small tetragonal elongation
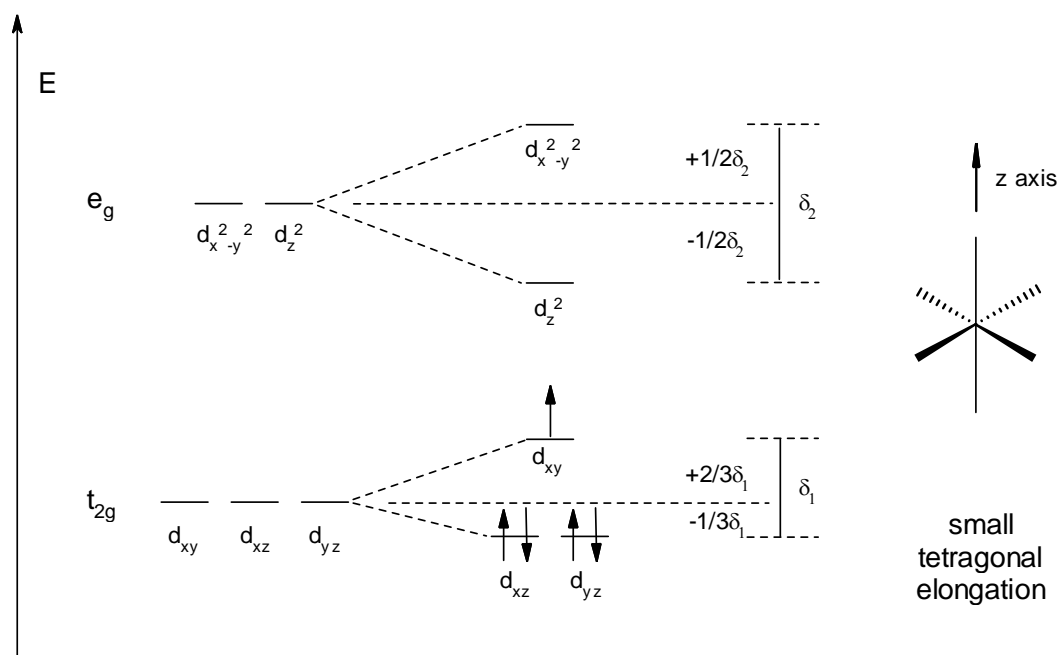
Figure A3. Jahn-Teller effect for $t_{2g}^3 e_g^1$ configuration leading to large tetragonal distortion. It should be noted, that due to symmetric splitting of e_g orbitals the type of distortion (compression or elongation) for this configuration can't be straightforwardly predicted from the simple symmetry and energy conservation considerations. Our calculation however revealed occurrence of a tetragonal elongation in $[Mn(H_2O)_6]^{3+}$ molecule.

Figure A4. Jahn-Teller effect for $t_{2g}^4 e_g^2$ configuration leads to small tetragonal compression

Figure A5. Jahn-Teller effect for $t_{2g}^5 e_g^0$ configuration leads to small tetragonal elongation

E

e_g

$d_{x^2-y^2}$ d_z^2

$d_{x^2-y^2}$ $+1/2\delta_2$

δ_2

$-1/2\delta_2$

d_z^2

z axis

t_{2g}

d_{xy} d_{xz} d_{yz}

d_{xy} $+2/3\delta_1$

δ_1

$-1/3\delta_1$

d_{xz} d_{yz}

small tetragonal elongation

Table A1. Imaginary frequencies of the transition metal (II) complexes in vacuum geometry with applied (O-metal-O) bond angle constraints; lowest frequency for each complex, which was used to replace the energy contribution from the imaginary frequencies; associated energy correction terms; and the resulting total vibrational correction energy accounting for all imaginary frequency modes. Frequencies are given in units of [cm^{-1}], while energies are in units of [kcal·mol^{-1}].

compound	squared frequencies	lowest real frequency	zero point energy	correction to vibrational energy [a]			total energy
				thermal enthalpy	thermal entropy	thermal free energy	
$[Mn(H_2O)_6]^{2+}$	-172.97 -152.21 -37.53	38.04	0.163	1.618	0.016	-3.172	-3.009
$[Fe(H_2O)_6]^{2+}$	-173.71 -81.19 -62.91	58.64	0.251	1.537	0.013	-2.488	-2.236
$[Ni(H_2O)_6]^{2+}$	-183.03 -20.61	67.83	0.194	1.001	0.008	-1.511	-1.317
$[Zn(H_2O)_6]^{2+}$	-159.62 -86.99 -55.84	47.12	0.202	1.582	0.015	-2.829	-2.627

[a] corrections are calculated according to eqs. (9) - (12) in the main text.

Table A2. Metal to oxygen (M–O) and oxygen to hydrogen (O–H) bond lengths in [Å] for protonated and deprotonated species of transition metal complexes geometry optimized in vacuum.

compound	protonated form		deprotonated form					
	M–O [a]	O–H [a]	M–O$_{eq}$ [b]	M–O$_{ax}$ [c]	M–O$_h$ [d]	O–H$_{eq}$ [b]	O–H$_{ax}$ [c]	O–H$_h$ [d]
$[Sc(H_2O)_6]^{3+}$	2.14	0.98	2.21	2.27	1.81	0.97	0.97	0.97
$[Ti(H_2O)_6]^{3+}$	2.08	0.98	2.16	2.20	1.75	0.97	0.97	0.97
$[V(H_2O)_6]^{3+}$	2.04	0.98	2.10	2.21	1.76	0.97	0.97	0.97
$[Cr(H_2O)_6]^{3+}$	2.01	0.98	2.05	2.16	1.79	0.97	0.97	0.97
$[Mn(H_2O)_6]^{3+}$ [e]	2.18 ax 1.97 eq	0.98 ax 0.98 eq	2.15	2.07	1.75	0.97	0.97	0.98
$[Fe(H_2O)_6]^{3+}$	2.06	0.98	2.14	2.16	1.75	0.97	0.97	0.97
$[Co(H_2O)_6]^{3+}$ [f]	1.94	0.98	2.12	2.10	1.74	0.97	0.97	0.98
$[Co(H_2O)_6]^{3+}$ [g]			1.94	2.05	1.80	0.98	0.97	0.97
$[Ru(H_2O)_6]^{3+}$	2.09	0.98	2.13	2.23	1.89	0.97	0.97	0.98
$[Rh(H_2O)_6]^{3+}$	2.08	0.98	2.08	2.22	1.95	0.98	0.97	0.97
$[Mn(H_2O)_6]^{2+}$	2.22	0.97	2.27	2.26	1.92	0.97	0.97	0.96
$[Fe(H_2O)_6]^{2+}$ [e]	2.19 ax 2.15 eq	0.97 ax 0.97 eq	2.22	2.20	1.92	0.97	0.97	0.96
$[Ni(H_2O)_6]^{2+}$	2.09	0.97	2.13	2.15	1.91	0.97	0.97	0.96
$[Zn(H_2O)_6]^{2+}$	2.15	0.97	2.22	2.14	1.91	0.97	0.97	0.96

[a] average metal to oxygen and oxygen to hydrogen bond lengths.
[b] average metal to oxygen and oxygen to hydrogen bond lengths for the equatorial water ligands.
[c] average metal to oxygen and oxygen to hydrogen bond lengths for the axial water ligand.
[d] metal to oxygen and oxygen to hydrogen bond lengths for the deprotonated water ligand.
[e] bond lengths for axial and equatorial ligands are given separately and denoted with ax or eq superscripts, respectively.
[f] computed for high spin deprotonated state.
[g] computed for low spin deprotonated state.

Table A3. Metal to oxygen (M–O) and oxygen to hydrogen (O–H) bond lengths in [Å] for protonated and deprotonated species of transition metal complexes geometry optimized in presence of explicit water.

compound	protonated form		deprotonated form					
	M–O [a]	O–H [a]	M–O$_{eq}$ [b]	M–O$_{ax}$ [c]	M–O$_h$ [d]	O–H$_{eq}$ [b]	O–H$_{ax}$ [c]	O–H$_h$ [d]
$[Sc(H_2O)_6]^{3+}$	2.11	0.99	2.17	2.19	1.85	0.98	0.99	0.96
$[Ti(H_2O)_6]^{3+}$	2.04	1.00	2.13	2.15	1.77	0.99	0.98	0.96
$[V(H_2O)_6]^{3+}$	2.01	0.99	2.06	2.17	1.79	0.98	0.98	0.97
$[Cr(H_2O)_6]^{3+}$	1.98	1.00	2.02	2.11	1.81	0.98	0.99	0.97
$[Mn(H_2O)_6]^{3+}$ [e]	2.15 ax 1.95 eq	0.98 ax 1.00 eq	2.12	2.04	1.76	0.98	0.99	0.97
$[Fe(H_2O)_6]^{3+}$	2.02	0.99	2.09	2.15	1.79	0.98	0.98	0.97
$[Co(H_2O)_6]^{3+}$ [f]	1.91	0.99	2.08	2.12	1.80	0.98	0.98	0.97
$[Co(H_2O)_6]^{3+}$ [g]			1.92	1.99	1.81	0.99	0.99	0.97
$[Ru(H_2O)_6]^{3+}$	2.07	0.99	2.10	2.17	1.92	0.99	0.99	0.97
$[Rh(H_2O)_6]^{3+}$	2.05	1.00	2.07	2.17	1.95	0.99	0.99	0.97
$[Mn(H_2O)_6]^{2+}$	2.20	0.98	2.26	2.22	2.01	0.98	0.98	0.96
$[Fe(H_2O)_6]^{2+}$ [e]	2.14 ax 2.14 eq	0.98 ax 0.98 eq	2.22	2.15	1.94	0.98	0.98	0.97
$[Ni(H_2O)_6]^{2+}$	2.08	0.98	2.12	2.11	1.96	0.98	0.98	0.97
$[Zn(H_2O)_6]^{2+}$	2.13	0.98	2.13	2.12	1.95	0.98	0.98	0.97

[a] average metal to oxygen and oxygen to hydrogen bond lengths.
[b] average metal to oxygen and oxygen to hydrogen bond lengths for the equatorial water ligands.
[c] average metal to oxygen and oxygen to hydrogen bond lengths for the axial water ligand.
[d] metal to oxygen and oxygen to hydrogen bond lengths for the deprotonated water ligand.
[e] bond lengths for axial and equatorial ligands are given separately and denoted with ax or eq superscripts, respectively.
[f] computed for high spin deprotonated state.
[g] computed for low spin deprotonated state.

Table A4. RESP charges of transition metal (III) complexes based on model structures optimized in vacuum. Atomic partial charges are determined in vacuum ($\varepsilon = 1$) (first nine lines) and alternatively in dielectric continuum with $\varepsilon = 80$ (last nine lines). Charges of protonated and deprotonated complexes are given in the left and right part of the table, respectively.

compound	protonated form			deprotonated form						
	metal	O [a]	H [a]	metal	O_{eq} [b]	O_{ax} [c]	O_h [d]	H_{eq} [b]	H_{ax} [c]	H_h [d]
$[Sc(H_2O)_6]^{3+}$	2.31	-1.05	0.58	1.92	-0.91	-0.88	-1.10	0.51	0.50	0.61
$[Ti(H_2O)_6]^{3+}$	2.18	-1.02	0.58	1.71	-0.89	-0.79	-0.97	0.50	0.48	0.61
$[V(H_2O)_6]^{3+}$	2.11	-1.01	0.58	1.28	-0.78	-0.73	-0.76	0.49	0.46	0.51
$[Cr(H_2O)_6]^{3+}$	2.03	-0.99	0.58	1.31	-0.82	-0.74	-0.71	0.50	0.47	0.44
$[Mn(H_2O)_6]^{3+}$ [e]	1.95	-1.01 ax / -0.94 eq	0.56 ax / 0.58 eq	1.33	-0.83	-0.71	-0.63	0.49	0.47	0.45
$[Fe(H_2O)_6]^{3+}$	2.04	-0.99	0.57	1.37	-0.80	-0.74	-0.82	0.48	0.46	0.58
$[Co(H_2O)_6]^{3+}$	1.70	-0.92	0.57	1.23	-0.81	-0.68	-0.64	0.48	0.45	0.55
$[Ru(H_2O)_6]^{3+}$	1.80	-0.94	0.57	1.10	-0.75	-0.76	-0.66	0.49	0.48	0.45
$[Rh(H_2O)_6]^{3+}$	1.20	-0.76	0.53	1.07	-0.74	-0.73	-0.67	0.50	0.47	0.40
$[Sc(H_2O)_6]^{3+}$	1.88	-0.94	0.57	1.47	-0.86	-0.83	-0.97	0.53	0.50	0.55
$[Ti(H_2O)_6]^{3+}$	1.94	-0.98	0.58	1.35	-0.84	-0.77	-0.87	0.52	0.49	0.56
$[V(H_2O)_6]^{3+}$	1.75	-0.92	0.57	1.44	-0.86	-0.86	-0.91	0.53	0.51	0.54
$[Cr(H_2O)_6]^{3+}$	1.40	-0.83	0.55	1.49	-0.89	-0.87	-0.93	0.54	0.52	0.51
$[Mn(H_2O)_6]^{3+}$ [e]	1.40	-0.88 ax / -0.80 eq	0.53 ax / 0.55 eq	1.42	-0.87	-0.83	-0.84	0.53	0.52	0.53
$[Fe(H_2O)_6]^{3+}$	1.49	-0.85	0.55	1.20	-0.82	-0.76	-0.77	0.52	0.49	0.54
$[Co(H_2O)_6]^{3+}$	1.19	-0.79	0.55	1.14	-0.82	-0.73	-0.65	0.51	0.49	0.55
$[Ru(H_2O)_6]^{3+}$	1.44	-0.86	0.56	1.42	-0.90	-0.93	-0.86	0.54	0.54	0.50
$[Rh(H_2O)_6]^{3+}$	1.38	-0.85	0.56	1.32	-0.86	-0.89	-0.89	0.55	0.53	0.48

[a] average charge of the oxygen and hydrogen atoms of water ligands.

[b] average charge on the oxygen or hydrogen atoms for equatorial water ligands.

[c] charge on the oxygen or hydrogen atoms for the axial water ligand.

[d] charge on the oxygen or hydrogen atom for the deprotonated water ligand.

[e] charges for axial and equatorial ligands are given separately and denoted with ax or eq superscripts, respectively.

Table A5. RESP charges of transition metal (III) complexes based on model structures optimized in presence of explicit solvent using a QM/MM approach. Atomic partial charges are determined in vacuum (first nine lines) and alternatively in dielectric continuum with $\varepsilon = 80$ (last nine lines). Charges of protonated and deprotonated complexes are given in the left and right part of the table, respectively.

compound	protonated form			deprotonated form						
	metal	O [a]	H [a]	metal	O_{eq} [b]	O_{ax} [c]	O_h [d]	H_{eq} [b]	H_{ax} [c]	H_h [d]
$[Sc(H_2O)_6]^{3+}$	2.11	-0.97	0.56	1.80	-0.90	-0.76	-1.03	0.51	0.46	0.58
$[Ti(H_2O)_6]^{3+}$	2.15	-1.01	0.57	1.60	-0.84	-0.77	-0.97	0.49	0.48	0.60
$[V(H_2O)_6]^{3+}$	1.81	-0.91	0.55	1.39	-0.85	-0.75	-0.70	0.51	0.46	0.45
$[Cr(H_2O)_6]^{3+}$	1.47	-0.80	0.53	1.55	-0.91	-0.78	-0.71	0.53	0.47	0.42
$[Mn(H_2O)_6]^{3+}$ [e]	1.44	-0.94 ax / -0.72 eq	0.55 ax / 0.52 eq	1.42	-0.86	-0.74	-0.63	0.50	0.47	0.46
$[Fe(H_2O)_6]^{3+}$	1.61	-0.84	0.53	1.15	-0.73	-0.70	-0.72	0.47	0.46	0.51
$[Co(H_2O)_6]^{3+}$	1.20	-0.77	0.53	1.44	-0.90	-0.80	-0.55	0.51	0.48	0.48
$[Ru(H_2O)_6]^{3+}$	1.29	-0.77	0.53	0.95	-0.67	-0.66	-0.64	0.46	0.45	0.43
$[Rh(H_2O)_6]^{3+}$	0.92	-0.66	0.50	0.94	-0.67	-0.64	-0.67	0.47	0.46	0.45
$[Sc(H_2O)_6]^{3+}$	2.04	-0.99	0.58	1.73	-0.95	-0.89	-1.06	0.55	0.53	0.56
$[Ti(H_2O)_6]^{3+}$	1.83	-0.95	0.57	1.50	-0.90	-0.78	-0.94	0.53	0.50	0.57
$[V(H_2O)_6]^{3+}$	1.71	-0.92	0.57	1.50	-0.89	-0.87	-0.92	0.54	0.52	0.51
$[Cr(H_2O)_6]^{3+}$	1.65	-0.90	0.56	1.57	-0.91	-0.90	-0.94	0.55	0.53	0.49
$[Mn(H_2O)_6]^{3+}$ [e]	1.63	-0.96 ax / -0.87 eq	0.55 ax / 0.57 eq	1.52	-0.92	-0.84	-0.84	0.53	0.53	0.51
$[Fe(H_2O)_6]^{3+}$	1.65	-0.89	0.56	1.50	-0.90	-0.86	-0.90	0.54	0.51	0.55
$[Co(H_2O)_6]^{3+}$	1.46	-0.88	0.57	1.48	-0.93	-0.88	-0.76	0.54	0.52	0.53
$[Ru(H_2O)_6]^{3+}$	1.49	-0.88	0.57	1.35	-0.88	-0.88	-0.85	0.54	0.53	0.49
$[Rh(H_2O)_6]^{3+}$	1.37	-0.85	0.56	1.27	-0.84	-0.89	-0.89	0.54	0.54	0.48

[a] average charge of the oxygen and hydrogen atoms of water ligands.
[b] average charge on the oxygen or hydrogen atoms for equatorial water ligands.
[c] charge on the oxygen or hydrogen atoms for the axial water ligand.
[d] charge on the oxygen or hydrogen atom for the deprotonated water ligand.
[e] charges for axial and equatorial ligands are given separately and denoted with ax or eq superscripts, respectively.

Table A6. RESP charges of transition metal (II) complexes based on model structures optimized in vacuum constraining (O-metal-O) bond angles between neighbor water ligands to 90°. Atomic partial charges are determined in vacuum ($\varepsilon = 1$) (first four lines) and alternatively in dielectric continuum with $\varepsilon = 80$ (last four lines). Charges of protonated and deprotonated complexes are given in the left and right part of the table, respectively.

compound	protonated form			deprotonated form						
	metal	O [a]	H [a]	metal	O_{eq} [b]	O_{ax} [c]	O_h [d]	H_{eq} [b]	H_{ax} [c]	H_h [d]
$[Mn(H_2O)_6]^{2+}$	1.75	-0.99	0.52	1.49	-0.90	-0.84	-1.16	0.46	0.46	0.50
$[Fe(H_2O)_6]^{2+}$ [e]	1.67	-1.00 ax / -0.97 eq	0.52 ax / 0.52 eq	1.33	-0.87	-0.82	-1.02	0.46	0.45	0.42
$[Ni(H_2O)_6]^{2+}$	1.65	-0.98	0.52	1.26	-0.84	-0.83	-0.99	0.45	0.46	0.41
$[Zn(H_2O)_6]^{2+}$	1.74	-0.99	0.52	1.42	-0.88	-0.79	-1.06	0.46	0.45	0.41
$[Mn(H_2O)_6]^{2+}$	1.36	-0.94	0.52	1.33	-0.98	-0.90	-1.14	0.52	0.51	0.47
$[Fe(H_2O)_6]^{2+}$ [e]	1.30	-0.95 ax / -0.92 eq	0.52 ax / 0.52 eq	1.38	-0.98	-0.96	-1.18	0.52	0.52	0.46
$[Ni(H_2O)_6]^{2+}$	1.27	-0.92	0.52	1.35	-0.96	-0.95	-1.19	0.52	0.52	0.46
$[Zn(H_2O)_6]^{2+}$	1.35	-0.94	0.53	1.42	-0.98	-0.94	-1.24	0.52	0.52	0.48

[a] average charge of the oxygen and hydrogen atoms of water ligands.
[b] average charge on the oxygen or hydrogen atoms for equatorial water ligands.
[c] charge on the oxygen or hydrogen atoms for the axial water ligand.
[d] charge on the oxygen or hydrogen atom for the deprotonated water ligand.
[e] charges for axial and equatorial ligands are given separately and denoted with ax or eq superscripts, respectively.

Table A7. RESP charges of transition metal (II) complexes based on model structures optimized in presence of explicit solvent using a QM/MM approach. Atomic partial charges are determined in vacuum (ε = 1) (first four lines) and alternatively in dielectric continuum with ε = 80 (last four lines). Charges of protonated and deprotonated complexes are given in the left and right part of the table, respectively.

compound	protonated form			deprotonated form						
	metal	O [a]	H [a]	metal	O_{eq} [b]	O_{ax} [c]	O_h [d]	H_{eq} [b]	H_{ax} [c]	H_h [d]
$[Mn(H_2O)_6]^{2+}$	1.55	-0.91	0.49	1.11	-0.78	-0.65	-0.92	0.43	0.40	0.36
$[Fe(H_2O)_6]^{2+}$ [e]	1.50	-0.96 [ax] / -0.89 [eq]	0.52 [ax] / 0.49 [eq]	0.97	-0.75	-0.67	-0.84	0.42	0.42	0.35
$[Ni(H_2O)_6]^{2+}$	1.29	-0.85	0.48	0.91	-0.74	-0.65	-0.86	0.42	0.40	0.35
$[Zn(H_2O)_6]^{2+}$	1.61	-0.94	0.50	1.08	-0.78	-0.67	-0.94	0.43	0.41	0.36
$[Mn(H_2O)_6]^{2+}$	1.43	-0.96	0.53	1.24	-0.92	-0.82	-1.15	0.50	0.48	0.44
$[Fe(H_2O)_6]^{2+}$ [e]	1.36	-0.96 [ax] / -0.94 [eq]	0.53 [ax] / 0.53 [eq]	1.19	-0.90	-0.91	-1.09	0.49	0.51	0.44
$[Ni(H_2O)_6]^{2+}$	1.36	-0.95	0.53	1.17	-0.91	-0.83	-1.12	0.50	0.48	0.42
$[Zn(H_2O)_6]^{2+}$	1.54	-1.00	0.54	1.29	-0.94	-0.85	-1.19	0.51	0.49	0.45

[a] average charge of the oxygen and hydrogen atoms of water ligands.

[b] average charge on the oxygen or hydrogen atoms for equatorial water ligands.

[c] charge on the oxygen or hydrogen atoms for the axial water ligand.

[d] charge on the oxygen or hydrogen atom for the deprotonated water ligand.

[e] charges for axial and equatorial ligands are given separately and denoted with ax or eq superscripts, respectively.

Table A8. Comparison of computed gas phase free energy of deprotonated hexa-aqua Co(III) complex in high spin state, based on the ground state electronic energies evaluated with restricted open shell DFT (RODFT) or unrestricted DFT (UDFT) formalisms, based on the vacuum (QM) and QM/MM geometry models. Geometries in all cases are optimized using the UDFT approach. Energies are given in [kcal·mol^{-1}] units.

DFT formalism	G_g with QM	G_g with QM/MM
RODFT	-378188.18	-378174.14
UDFT	-378192.02	-378178.07
difference	3.84	3.93

Table A9. Formal theoretical and computed expectation values of the total spin S^2 operator for ground state electronic energy computations performed using unrestricted DFT approach. The deviations from theoretical values remained in the same range in the course of geometry optimizations.

compound	total spin S^2		
	formal [a]	Computed	
		QM	QM/MM
$[Ti(H_2O)_6]^{3+}$	0.750	0.751	0.751
$[Ti(H_2O)_5OH]^{2+}$		0.753	0753
$[V(H_2O)_6]^{3+}$	2.000	2.004	2.004
$[V(H_2O)_5OH]^{2+}$		2.014	2.014
$[Cr(H_2O)_6]^{3+}$	3.750	3.759	3.759
$[Cr(H_2O)_5OH]^{2+}$		3.764	3.765
$[Mn(H_2O)_6]^{3+}$	6.000	6.019	6.023
$[Mn(H_2O)_5OH]^{2+}$		6.068	6.060
$[Fe(H_2O)_6]^{3+}$	8.750	8.756	8.756
$[Fe(H_2O)_5OH]^{2+}$		8.761	8.760
$[Co(H_2O)_5OH]^{2+}$	6.000	6.013	6.012
$[Ru(H_2O)_6]^{3+}$	0.750	0.755	0.753
$[Ru(H_2O)_5OH]^{2+}$		0.753	0.753
$[Mn(H_2O)_6]^{2+}$	8.750	8.752	8.753
$[Mn(H_2O)_5OH]^{+}$		8.754	8.754
$[Fe(H_2O)_6]^{2+}$	6.000	6.005	6.005
$[Fe(H_2O)_5OH]^{+}$		6.007	6.006
$[Ni(H_2O)_6]^{2+}$	2.000	2.002	2.002
$[Ni(H_2O)_5OH]^{+}$		2.003	2.003

[a] formal theoretical total spin is calculated as *s(s+1)*, where *s* equals to 0.5 times the number of unpaired electrons.

Table A10. Computed values for the energy terms ΔG_g, $\Delta\Delta G_{solv}$, ΔG_{aq}, used in calculations of the $pK_A^{(micro)}$ values for vacuum (QM) and QM/MM geometry models. Electronic energies are evaluated using quadruple–ζ basis set as described in the Methods Section. All energies are given in [kcal·mol⁻¹].

compound	QM			QM/MM		
	ΔG_g	$\Delta\Delta G_{solv}$	ΔG_{aq}	ΔG_g	$\Delta\Delta G_{solv}$	ΔG_{aq}
$[Sc(H_2O)_6]^{3+}$	22.17	-14.79	7.37	20.88	-15.19	5.69
$[Ti(H_2O)_6]^{3+}$	12.79	-8.48	4.31	10.30	-7.81	2.49
$[V(H_2O)_6]^{3+}$	16.43	-8.74	7.68	11.46	-6.65	4.81
$[Cr(H_2O)_6]^{3+}$	21.28	-9.39	11.89	13.49	-6.39	7.10
$[Mn(H_2O)_6]^{3+}$	6.67	-6.59	0.07	-2.20	-1.85	-4.05
$[Fe(H_2O)_6]^{3+}$	12.61	-6.69	5.91	11.72	-8.79	2.93
$[Co(H_2O)_6]^{3+}$ [a]	-4.68	8.93	4.25	-5.07	8.86	3.80
$[Co(H_2O)_6]^{3+}$ [b]	11.26	-6.12	5.14	6.35	-0.22	6.13
$[Ru(H_2O)_6]^{3+}$	22.01	-14.48	7.54	19.58	-13.30	6.28
$[Rh(H_2O)_6]^{3+}$	19.30	-14.43	4.87	12.62	-8.06	4.56
$[Mn(H_2O)_6]^{2+}$	153.76	-135.30	18.46	155.99	-141.84	14.15
$[Fe(H_2O)_6]^{2+}$	157.07	-140.36	16.71	146.86	-133.29	13.57
$[Ni(H_2O)_6]^{2+}$	154.03	-140.60	13.42	148.76	-134.08	14.68
$[Zn(H_2O)_6]^{2+}$	155.22	-141.23	14.00	154.54	-141.69	12.85
$[Co(H_2O)_6]^{3+}$ [c]	-8.52	8.93	0.41	-8.99	8.86	-0.13

[a] proper ΔG_g computed using restricted open shell DFT for the high spin deprotonated state. The protonated state is closed shell.
[b] energy terms computed assuming no spin state change upon deprotonation.
[c] ΔG_g computed using unrestricted DFT for the deprotonated state. The protonated state is closed shell. Not used in pK_A computations.

Table A11. Comparison of measured and computed pK$_A$ values for vacuum (QM) and QM/MM geometry models.

compound	measured [a]	pK$_A$ QM	QM/MM	ΔpK$_A$ (computed−measured) QM	QM/MM
$[Sc(H_2O)_6]^{3+}$	4.30	4.32	3.09	0.02	-1.21
$[Ti(H_2O)_6]^{3+}$	2.15	2.08	0.75	-0.07	-1.40
$[V(H_2O)_6]^{3+}$	2.60	4.55	2.44	1.95	-0.16
$[Cr(H_2O)_6]^{3+}$	4.20	7.63	4.12	3.43	-0.08
$[Mn(H_2O)_6]^{3+}$	0.08	-1.02	-4.05	-1.10	-4.13
$[Fe(H_2O)_6]^{3+}$	2.20	3.25	1.06	1.05	-1.14
$[Co(H_2O)_6]^{3+}$ [b]	2.90	2.04	1.70	-0.86	-1.20
$[Co(H_2O)_6]^{3+}$ [c]		2.69	3.41	-0.21	0.51
$[Ru(H_2O)_6]^{3+}$	2.47	4.44	3.52	1.97	1.05
$[Rh(H_2O)_6]^{3+}$	3.60	2.49	2.26	-1.11	-1.34
$[Mn(H_2O)_6]^{2+}$	10.60	12.45	9.28	1.85	-1.32
$[Fe(H_2O)_6]^{2+}$	9.50	11.17	8.86	1.67	-0.64
$[Ni(H_2O)_6]^{2+}$	9.90	8.75	9.67	-1.15	-0.23
$[Zn(H_2O)_6]^{2+}$	9.50	9.18	8.34	-0.32	-1.16
RMSD [d]				**1.2**	**1.0**

[a] measured pK$_A$ values are adopted from the Ref.(Gilson and Durrant 2009)
[b] computed using restricted open shell DFT for the high spin deprotonated state. The protonated state is closed shell.
[c] computed assuming no spin state change upon deprotonation.
[d] RMS errors don't include outliers, Cr(III) and Mn(III) complexes for QM and QM/MM geometry models, respectively.

Table A12. Comparison of gas phase, solvation and aqueous free energies (shown in [kcal·mol^{-1}] units) of two different distorted geometries with tetragonal elongation or compression found for hexa-aqua Mn(III) complex with geometries modeled in vacuum shown in Fig. 7.

distortion	G_g [a]	ΔG_{solv} [b]	$G_{aq} = G_g + \Delta G_{solv}$
elongation	-352416.62	-480.56	-352897.19
compression	-352416.07	-479.97	-352896.04
difference	-0.55	-0.59	-1.15

[a] calculated according to eq. (5) in the main text.
[b] calculated solving Poisson equation.
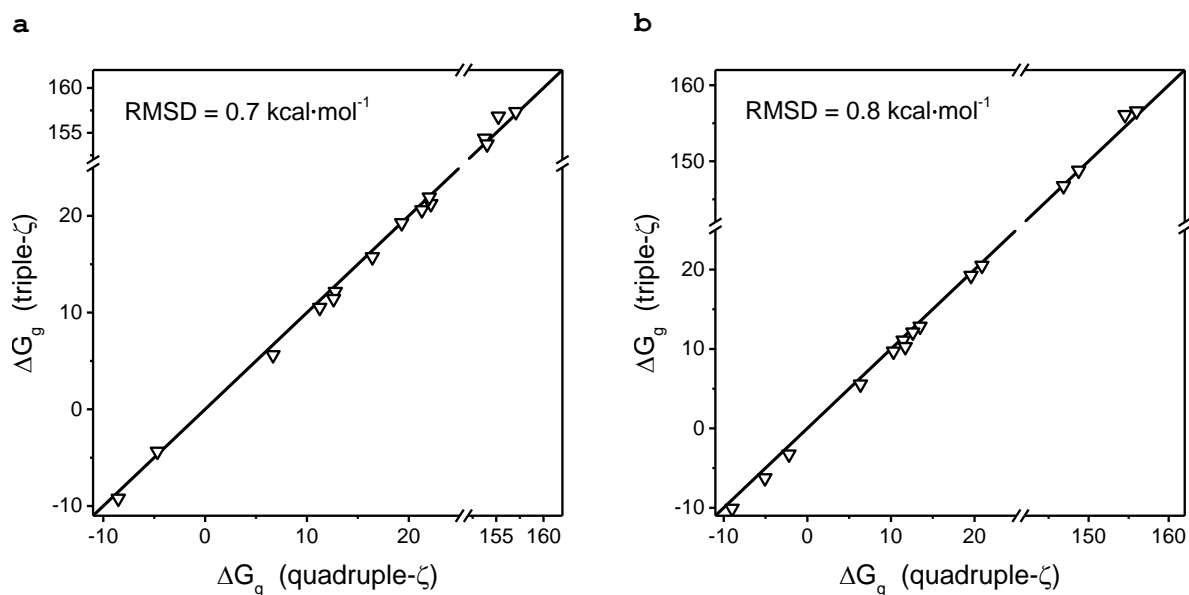
Figure A6. Comparison of 15 gas-phase basicities (ΔG_g) based on the ground state electronic energies computed with quadruple–ζ (Table S10) or triple–ζ basis sets (Table S12), for geometries optimized **a:** in vacuum and **b:** in presence of explicit solvent. Energies are given in kcal·mol^{-1}.

Table A13. Gas phase basicities ΔG_g of studied compounds computed using cc–pVTZ basis set of triple–ζ quality for O and H atoms, for vacuum (QM) and QM/MM geometry models. Metals are described as defined in the methods part of the main text of this article. All energies are given in [kcal·mol^{-1}] units.

compound	ΔG_g	
	QM	QM/MM
$[Sc(H_2O)_6]^{3+}$	21.83	20.51
$[Ti(H_2O)_6]^{3+}$	12.16	9.70
$[V(H_2O)_6]^{3+}$	15.75	10.59
$[Cr(H_2O)_6]^{3+}$	20.60	12.84
$[Mn(H_2O)_6]^{3+}$	5.62	-3.26
$[Fe(H_2O)_6]^{3+}$	11.62	10.67
$[Co(H_2O)_6]^{3+\ a}$	-4.36	-6.25
$[Co(H_2O)_6]^{3+\ b}$	10.51	5.55
$[Ru(H_2O)_6]^{3+}$	21.92	19.24
$[Rh(H_2O)_6]^{3+}$	19.17	12.11
$[Mn(H_2O)_6]^{2+}$	154.38	156.60
$[Fe(H_2O)_6]^{2+}$	157.33	146.77
$[Ni(H_2O)_6]^{2+}$	153.94	148.80
$[Zn(H_2O)_6]^{2+}$	156.83	156.11
$[Co(H_2O)_6]^{3+\ c}$	-9.21	-10.10

[a] computed using restricted open shell DFT for the high spin deprotonated state. The protonated state is closed shell.
[b] computed assuming no spin state change upon deprotonation.
[c] computed using unrestricted DFT for the deprotonated state. The protonated state is closed shell.

Table A14. Measured electron affinities (EA) for metal (III) ions considered in this work.

metal ion	EA [a]
Sc^{3+}	-24.757
Ti^{3+}	-27.492
V^{3+}	-29.311
Cr^{3+}	-30.960
Mn^{3+}	-33.668
Fe^{3+}	-30.652
Co^{3+}	-33.500
Ru^{3+}	-28.470
Rh^{3+}	-31.060

[a] EA of M^{3+} ion equals to the negative of first ionization potential (IP) of M^{2+} ion. Corresponding measured IP values are adopted from (David R. Lide, ed., CRC Handbook of Chemistry and Physics, Internet Version 2005, CRC Press, Boca Raton, FL, 2005.)
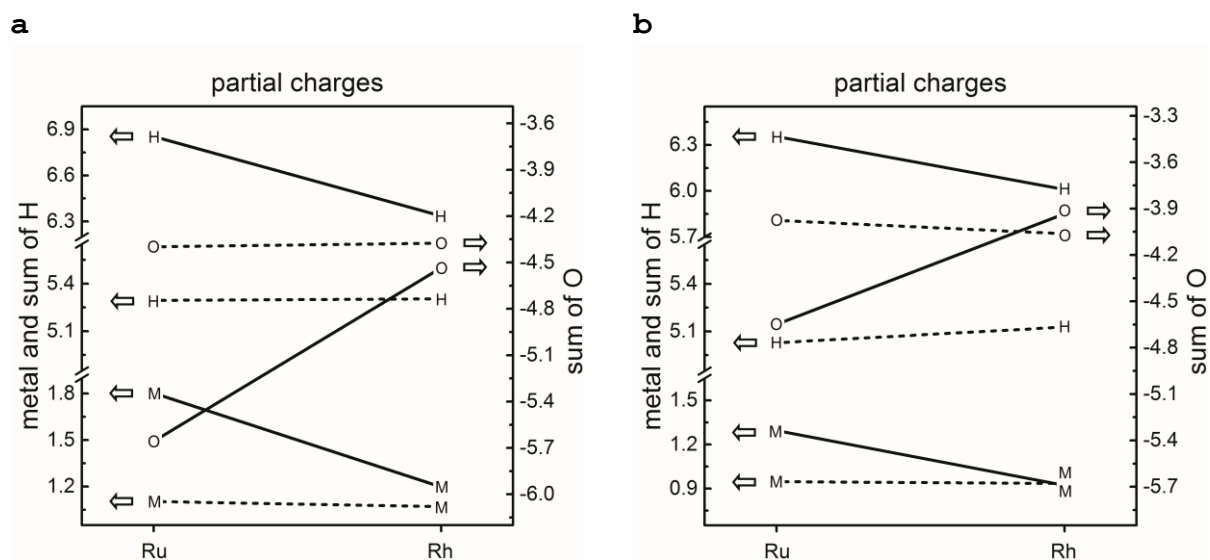
Figure A7. Partial charge of metal, net partial charges of hydrogen and oxygen atoms computed in vacuum for **a:** vacuum and **b:** QM/MM geometries of protonated (solid lines) and deprotonated (dashed lines) species of second-row transition metal (III) complexes.
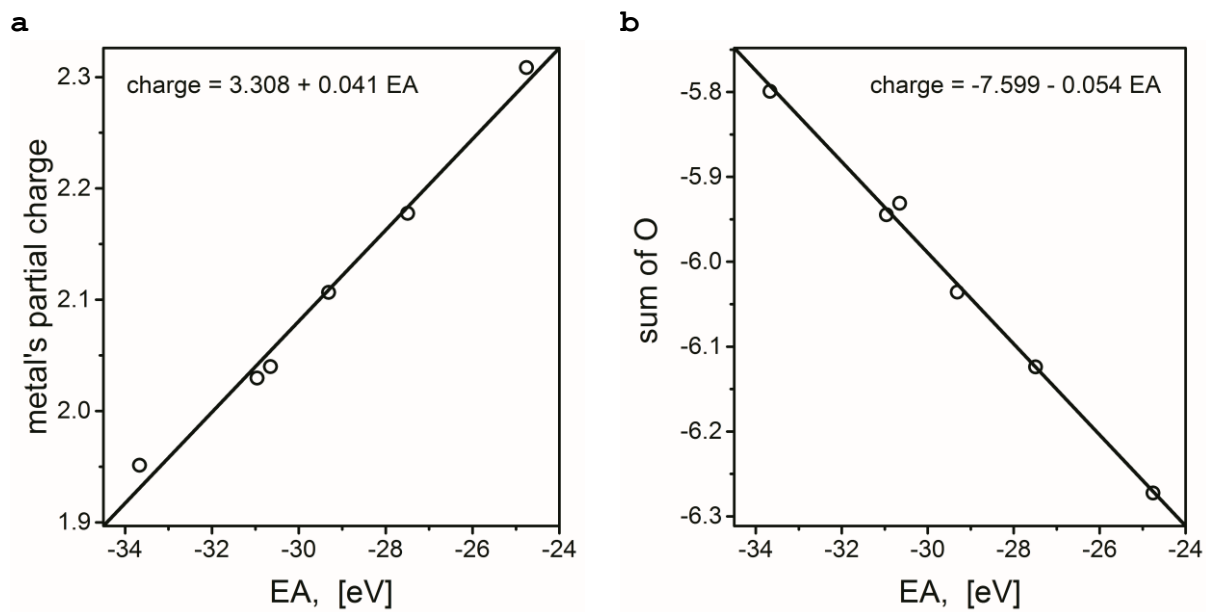
Figure A8. Correlation between measured EA of M^{3+} ion and RESP charge of **a:** metal center or **b:** oxygens in protonated complexes of metals from Sc(III) to Fe(III).